AD-A257 799

(1)

DARPA/ONR Grant #N00014-91-J-1976

Fifth Quarterly Progress Report
(covering the period of August 1 - October 31, 1992)

Project Title: Development of Ultra-Low Noise, High Sensitivity Planar Metal Grating Coupled AlGaAs/GaAs Multiquantum Well IR Detectors for Focal Plane Array Staring IR Sensor Systems

Submitted to

Max N. Yoder
Office of Naval Research
Code 1114 SS
800 North Quincy Street
Arlington, VA 22217-5000

DTIC
ELECTE
NOV 16 1992
S B D

Prepared by

Prof. Sheng S. Li

Dept. of Electrical Engineering
University of Florida
Gainesville, Florida 32611

Tel.(904)-392-4937
Fax(904)-392-8671

DISTRIBUTION STATEMENT A
Approved for public release
Distribution Unlimited

November 10, 1992

404525

92-29484

92 11 12 130

Fifth Quarterly Progress Report: August 1 - October 31, 1992

Project Title: Development of ultra-low noise high-detectivity planar metal grating coupled III-V multiquantum-well/superlattice barrier infrared photodetectors for focal plane array (FPA) staring infrared sensor systems.

Program Manager: Max N. Yoder, Office of Naval Research, Code 1114SS,Arlington, VA 22217.

Principal Investigator: Sheng S. Li, Professor, University of Florida, Gainesville, FL 32611.

Project Objectives:

1. To develop ultra-low dark current and high detectivity planar metal grating coupled bound-to-miniband (BTM) III-V quantum well infrared photodetectors (QWIPs) for 8 to 12 μm focal plane array (FPA) staring IR sensor systems.

2. To develop novel type-I and tyep-II III-V QWIPs with multicolor, broad and narrow band spectral response in the 8 to 14μm wavelength range. The material systems to be studied include GaAs/AlGaAs, AlAs/AlGaAs, and InGaP/GaAs grown on GaAs substrates, and InAlAs/InGaAs grown on InP substrate.

3. To conduct theoretical and experimental studies of the planar metal grating-coupled structures for normal incident illumination on the QWIPs. Different metal grating coupling structures using 1-D (line) and 2-D (square) metal gratings for the QWIPs will be studied in order to achieve high coupling efficiency under normal front- and back-illuminations.

4. To perform theoretical and experimental studies of dark current, photocurrent, optical absorption, spectral responsivity, noise, and detectivity in different types of QWIPs developed under this program.

DTIC QUALITY INSPECTED 4

I. Introduction

During this reporting period (8-01-92 to 10-31-92) we have continued to make significant progress towards the program goals. We have designed, fabricated, and characterized several new

ADA254697
Codes
Avail and/or
Dist Special
A-1

types of metal grating coupled GaAs/AlGaAs, AlAs/AlGaAs, and InAlAs/InGaAs QWIPs for 8 - 12 μm focal plane array (FPA) staring infrared sensor applications. Specific tasks performed during this period include: (i) designed, fabricated, and characterized new bound-to-miniband (BTM) transition GaAs/AlGaAs QWIPs with two different well doping densities, (ii) completed characterization of the normal incidence type-II indirect gap AlAs/AlGaAs QWIPs grown on the (110) GaAs substrate, (iii) developed a new dual-mode (photovoltaic (PV) and photoconductive (PC)) two-color GaAs/AlGaAs QWIPs with two-band spectral response (6 to 9 μm and 9 -16 μm), (iv) developed a new voltage-tunable dual-mode (PV and PC) detection InAlAs/InGaAs BTM QWIP with narrow- and broad-band spectral response around $\lambda_p = 10$ μm, and (v) completed the numerical simulation of quantum efficiency versus grating periodicity and wavelength for a two-dimensional (2-D) double-period square metal grating couplers for normal incident transmission and reflection mode illumination on the BTM QWIPs. Detailed results are discussed in Section 3.

II. Research Accomplishments and Publications

Specific accomplishments and publications during this period are summarized as follows:

2.1 Research Accomplishments:

1. Developed a new dual-mode (PV and PC) detection GaAs/AlGaAs QWIP using an enlarged-GaAs quantum well (110 Å) and AlGaAs barrier (875 Å) layer for the 6-9 and 9-16 μm wavelength IR detection. For the 6-9 μm wavelength detection, the detector operated in the PV mode detection by using the ground-state to continuum states transition. For the 9-16 μm detection, the QWIP operated in PC mode detection by using the first-excited state to continuum states transition. A responsivity of $R_A = 2$ mA/W and a detectivity of $D^* = 1.48\times10^9$ cm$\sqrt{Hz}$/W were obtained at $\lambda = 7.7\mu$m and T = 77 K for the PV mode operation. For the PC mode operation, $R_A = 0.49$ A/W and $D^* = 1\times10^{10}$ at $V_b = 2$ V were obtained at $\lambda = 12$ μm and T = 77 K. Detailed results have been discussed in the previous quarterly report and submitted for publication.

2. Developed a new voltage-tunable dual-mode (PV and PC) operation InAlAs/InGaAs BTM QWIP with narrow- and broad-band spectral response around $\lambda_p = 10$ μm. This BTM QWIP uses an $In_{0.53}Ga_{0.47}As$ quantum well (110 Å) and a short-period $In_{0.52}Al_{0.48}As/In_{0.53}Ga_{0.47}As$ (35/50 Å) superlattice barrier layer grown on InP substrate. The detectivity D* for this QWIP operating in PV and 'C mode was found to be $5.8 \times 10^9\ cm - \sqrt{Hz}/W$ at $V_b = 0$, and 0.5 V, and λ =10, and 10.3 μm, and T = 67 K. Detailed results are described in Section 3.1.

3. Completed detailed characterization of a normal incidence type-II QWIP using an indirect $Al_{0.5}Ga_{0.5}As/AlAs$ system grown on [110] GaAs substrate. A broad spectral response covering four different wavelength windows from 0.5 - 17 μm was observed in this new QWIPs. The dark current, optical absorption coefficient, responsivity, detectivity, and spectral response of this detector have been characterized. An ultra-large photocurrent gain (g = 100) was obtained in this QWIP at $\lambda = 2.2\mu$m. Detailed results are discussed in Section 3.2.

4. Completed numerical simulation of the 2-D square reflection and transmission metal grating structures formed on the GaAs/AlGaAs BTM QWIPs using the ***method of moment***. The advantages of these grating structures are for normal incident illumination and that the coupling of incident radiation is independent of the polarization direction. The results showed that a significant enhancement of light coupling efficiency by using the 2-D square grating structure operated in the transmission as well as the reflection modes. Based on the simulation results, it is possible to design and fabricate a variety of square grating couplers with excellent coupling efficiencies (15 to 25 %) in the 10 - 12 μm wavelength range. We will be fabricating the 2-D square grating coupler structures with different grating periods on the BTM QWIPs during the next reporting period to compare the coupling quantum efficiency versus grating period in these new structures. Detailed theoretical description of the ***method of moment*** and numerical simulation results for the 2-D square grating coupled BTM QWIPs are given in Section 3.3.

2.2. Refereed Journal Papers:

1. L. S. Yu and S. S. Li,"A Low Dark Current, High Detectivity Grating Coupled AlGaAs/GaAs Mulitple Quantum Well IR Detector Using Bound-to-Miniband Transition for 10 μm Detection,"Appl. Phys. Letts., 59 (11), p.1332, Sept.9, 1991.

2. L. S. Yu, S. S. Li, and Pin Ho "Largely Enhanced Bound-to-Miniband Absorption in an InGaAs Multiple Quantum Well with a Short-Period Superlattice InAlAs/InGaAs Barrier " Applied Phys. Letts., 59 (21), p.2712, Nov. 18, 1991.

3. L. S. Yu, Y. H. Wang, S. S. Li and Pin Ho,"A Low Dark Current Step-Bound-to-Miniband Transition InGaAs/GaAs/AlGaAs Multiquantum Well Infrared Detector," Appl. Phys. Letts., 60(8), p.992, Feb.24, 1992.

4. L. S. Yu, S. S. Li,and P. Ho,"A Normal Incident Type-II Quantum Well Infrared Detector Using an Indirect AlAs/$Al_{0.5}Ga_{0.5}As$ System Grown on [110] GaAs,"Electronics Letts , 28(15) p.1468, July,16, 1992.

5. L. S. Yu, S. S. Li, Y. H. Wang, and Y. C. Kao,"A Study of Coupling Efficiency versus Grating Periodicity in A Normal Incident Grating-Coupled GaAs/AlGaAs Quantum Well Infrared Detector," J. Appl. Phys., 72(6), pp.2105, Sept. 15, 1992.

6. Y. C. Wang and S. S. Li,"A Numerical Analysis of Double Periodic Reflection Metal Grating Coupler for Multiquantum Well Infrared Photodetectors," submitted to Journal Appl. Phys., Sept., 1992.

7. Y. H. Wang, S, S. Li, and P. Ho,"A Photovoltaic and Photoconductive Dual Mode Operation GaAs/AlGaAs Quantum Well Infrared Detector for Two Band Detection," accepted, Appl.Phys. Lett.,Jan. issue, 1993.

8. Y. H. Wang, S. S. Li, and P. Ho,"A Voltage-Tunable Dual Mode Operation InAlAs/InGaAs Bound-to-Miniband Transition QWIP for Narrow and Broad Band Detection at 10 μm," submitted to Appl. Phys. Lett., Sept., 1992.

9. P. Ho, P. A. Martin, L. S. Yu, and S. S. Li,"Growth of GaAs and AlGaAs on Misoriented (110) GaAs and a Normal Incidnece Type-II Quantum Well Infrared Detector," accepted, J. Vacuum Science and Technology, Oct., 1992.

10. S. S. Li, M. Y. Chuang and L. S. Yu,"Current Conduction Mechanisms in Bound-to-Miniband Transition III-V Quantum Well Infrared Photodetectors," accepted, ***Semiconductor Science and Technology***, Institute of Physics Publishing, Bristol, England, Oct., 1992.

2.3. Workshop and Conference Presentations

1. L. S. Yu, S. S. Li, and Pin Ho, " Largely Enhanced Intra-subband Absorption in a Wide InAlAS/InGaAs Quantum Well with a Short-Period Superlattice Barrier Structure,"paper presented at the ***SPIE's Symposium on Quantum Wells and Superlattices***, Somerset, NJ, 23-27 March,1992. Paper published in the SPIE Conference Proceeding.

2. S. S. Li and L. S. Yu, "Grating Coupled Bound-to-Miniband Transition III-V Quantum Well Infrared Detectors," **invited paper**, presented at ***the Innovative Long Wavelength Infrared Photodetector Workshop***, Jet Propulsion Lab., Pasadena, CA, April 7-9, 1992.

3. L. S. Yu and S. S. Li,"A Normal Incident Type-II Quantum Well Infrared Detector Using an Indirect AlAs/$Al_{0.5}Ga_{0.5}As$ System Grown on [110] GaAs, paper presented at ***the Innovative Long Wavelength Infrared Photodetector Workshop***, Jet Propulsion Lab., Pasadena, CA, April 7-9, 1992.

4. L. S. Yu, S. S. Li, Y. H. Wang, and P. Ho," Grating Coupled III-V Quantum Well Infrared Detectors Using Bound-to-Miniband Transition," paper presented at ***the SPIE Conference on Infrared Detectors and Focal Plane Arrays at OE/Aerospace Sensing 92***," Orlando, FL, April 20-24, 1992. Full paper published in the SPIE conference proceeding.

5. S. S. Li,"Grating Coupled Bound-to-Miniband Transition III-V Multiquantum Well Infrared Photodetectors," presented at the DARPA IR Detector Workshop, Washington D.C., June 12, 1992.

6. S. S. Li, M. Y. Chuang and L. S. Yu,"Current Conduction Mechanisms in Bound-to-Miniband Transition III-V Quantum Well Infrared Photodetectors," paper presented at the ***International Conference on Narrow Gap Semiconductors***, University of Southampton, Southampton, UK, July 19-23, 1992.

7. *P. Ho, P. A. Martin, L. S. Yu, and S. S. Li,*"Growth of GaAs and AlGaAs on Misoriented (110) GaAs and a Normal Incidnece Type-II Quantum Well Infrared Detector," paper presented at the 12th North American Conference on Molecular Beam Epitaxy," Oct.12-14, 1992.

8. S. S. Li, Y. H. Wang, M. Y. Chuang, P. Ho, and O. Manasreh, "A Normal Incidence Type-II AlAs/AlGaAs QWIP for Multicolor Infrared Detection," submitted to Materials Research Society, Symposium C2, **Infrared Detectors**, April 12 - 16, San Francisco, 1993.

2.4 Interactions with Government and Industrial Laboratories

1. Continued to collaborate with Dr. Pin Ho of General Electric Co.,in Syracuse, NY, on the growth of III-V QWIP's structures by using the molecular beam epitaxy (MBE) technique.

2. Continued to collaborate and exchange technical information on QWIP's research with Dr. Barry Levine of A T & T Bell Laboratories. Dr. Swami Swaminathan of A T & T Bell lab., in Breinigsville, PA, has expressed interest in collaboration with Dr. Li on the planar metal grating coupler structure developed at the University of Florida for possible applications in their QWIP focal plane arrays.

3. Dr. Li gave an invited talk at the Electronics Technology Laboratory, WRDC/ELRA, WPAFB, Ohio, on ***The bound-to-miniband transition III-V QWIPs*** on August 21, and discussed with Dr.Omar Manasreh and his colleagues in the Electronics Technology Laboratory at the Wright Patterson Air Force Base. Dr. Manasreh had performed optical absorption measurements on Dr. Li's QWIP samples, while Dr. Li has fabricated and characterized the QWIP samples provided by Dr. Manasreh.

4. Dr. Li was invited by American Engineering Education Association to serve on the review panel for Navel Postdoctoral Fellowship program in Washington D.C. August 7, to review a dozen proposals with other pannel members submitted by various applicants. Dr. Li was responsible for recommending one of the applicants whose proposal was on quantum well IR detector research.

III. Technical Results and Discussion

3.1 A Voltage-Tunable Dual-Mode Operation InAlAs/InGaAs BTM QWIP for 10 μm Detection

Summary: A new photoconductive (PC) and photovoltaic (PV) dual-mode operation quantum well infrared photodetector (QWIP) using a n-type $In_{0.52}Al_{0.48}As/In_{0.53}Ga_{0.47}As$ system grown on InP substrate has been developed for both narrow-band ($\Delta\lambda/\lambda_p = 7$ %) and broad-band ($\Delta\lambda/\lambda_p =$ 24 %) detection with a peak spectral response around $\lambda_p = 10$ μm. The detection scheme utilizes a voltage-tuned bound-to-miniband transition from the ground-state in the $In_{0.53}Ga_{0.47}As$(110 $\AA$) quantum well to the global miniband states in the InAlAs/InGaAs superlattice barrier layers. The detectivity D^*_λ for the PV mode operation was found to be 5.7×10^9 cm $\sqrt{Hz}$/W at $\lambda_p = 10$ μm and T = 67 K, while D^*_λ for the PC mode operation was found to be 5.8×10^9 $\sqrt{Hz}$/W at $V_b = 0.5$ V, $\lambda_p = 10.3$ μm and T = 67 K.

3.1.1 Introduction

The long-wavelength quantum well infrared photodetectors (QWIPs) based on intersubband transitions for detection in the 8 - 14 μm atmospheric window have been extensively investigated in recent years[1-11]. A great deal of the works have been reported on the GaAs/AlGaAs quantum well/superlattice infrared photodetectors using bound-to-bound[1-2], bound-to-miniband[3-5] and bound-to-continuum[6-7] conduction intersubband transitions. Studies of the intersubband absorption have also been conducted in the InGaAs/InAlAs system in the 3 to 5 μm wavelength range

[8–10]. Since the InAlAs/InGaAs heterostructure has a larger conduction band offset ($\Delta E_c \sim 500$ meV) compared to the GaAs/AlGaAs system, it is a promising candidate for both mid-wavelength infrared (MWIR) and long-wavelength infrared (LWIR) applications. Recently, we have reported the observation of a largely enhanced intersubband absorption in the InAlAs/InGaAs system using bound-to-miniband transition in the 8-14 μm[11] wavelength range. The results showed that multicolor (in the 3-5μm, 8-14 μm or even longer wavelength ($\sim$ 100 μm)) infrared detectors can be realized in the InAlAs/InGaAs system due to a much larger potential barrier (ΔE_c = 500 meV) created by using a short period superlattice barrier structure and resonant miniband conduction mechanism[11]. In addition, photovoltaic (PV) mode operation QWIPs using bound-to-miniband conduction[3,12,13] have been reported recently.

In this section we report a dual-mode (PV and PC) operation InAlAs/InGaAs multiple quantum well with superlattice barrier infrared photodetector (QWIP) using voltage-tuned bound-to-miniband transition mechanism. This new QWIP structure was grown on a lattice-matched semi-insulating (SI) InP substrate by using the molecular beam epitaxy (MBE) technique. A 1-μm $In_{0.53}Ga_{0.47}As$ buffer layer with doping density of 2×10^{18} cm^{-3} was first grown on the SI InP substrate, followed by the growth of 20 periods of enlarged $In_{0.53}Ga_{0.47}As$ quantum wells with a well width of 110 $\AA$ and a dopant density of 5×10^{17} cm^{-3}. The barrier layers on each side of the quantum well consist of 6 periods of undoped $In_{0.52}Al_{0.48}As$ (35 $\AA$)/$In_{0.53}Ga_{0.47}As$ (50 $\AA$) superlattice barrier layers. A 0.3 μm thick n^+-$In_{0.53}Ga_{0.47}As$ cap layer with a dopant density of 2×10^{18} cm^{-3} was grown on top of this QWIP structure for ohmic contacts. Figure 1 shows the energy band diagram for this BTM QWIP. The transition scheme for this QWIP is from the localized ground state level E_{EW1} in the enlarged well (EW) to the global resonant-coupled miniband E_{SL1} in the superlattice (SL) barrier layers. The physical parameters of the quantum well and superlattice barrier are chosen so that the first excited level E_{EW2} of the EW is merged and lined up with the ground level of the miniband E_{SL1} on both sides of the EW to obtain a maximum intersubband absorption strength.

3.1.2 Results and Discussion

The mesa structure for the InGaAs BTM QWIP was formed by chemical etching through the active layers and stopped at the n^+ GaAs buffer layer for ohmic contacts. The active area of the detector is $200\times200\mu m^2$. To enhance coupling efficiency for normal illumination and angular independent radiation polarization, a planar 2-D cross metal grating coupler was deposited on the

QWIP by using electron beam (E-beam) evaporation with 0.2μm AuGe/Ni/Au films. The 2-D cross metal grating coupler consists of equally spaced square shape metal gratings with a grating period Λ = 10 μm and a geometrical ratio factor g = d/Λ = 0.5, where d is the width of the square metal grating.

Numerical simulations of the energy states E_{EWn}, E_{SLn} (n = 1,2,...) and the transmission coefficient $T * T$ for the QWIP were carried out by using a multi-layer transfer matrix method (TMM)[3]. The results are shown in Fig.2 for V_b = 0, 0.5 V. In our design, a broad and highly degenerated miniband was formed by using the superlattice barrier structure. The center energy position of the first miniband is located at 163 meV above the conduction band edge of InGaAs EW with a bandwidth of $2\Gamma \sim 60$ meV. In order to determine accurately the intersubband transition levels, detailed calculations of the energy differences between the subband levels by taking into account the effects of band nonparabolicity[14], electron-electron interaction[15], and electron plasma[16] are needed. In analysing our QWIP, we have considered both electron-electron interaction (exchange energy) E_{xch} and depolarization E_{de} effects. The results showed a lowering of $\sim$5 meV for the heavily populated bound states E_{EW1} in the quantum well. The peak absorption wavelength can be found from the relation

$$\lambda_p = \frac{1.24}{E_{SL1} - E_{EW1} + E_{xch} - E_{de}} \quad (\mu m)$$

Now, substituting values of E_{SL1} = 163 meV, E_{EW1} = 51 meV, and E_{xch}-$E_{de} \sim$ 5 meV into the above equation, we obtain λ_p = 10.6 μm. The infrared intersubband absorption versus wavelength for this QWIP was measured at Brewster's angle[14] ($\theta_B = \sim 73^o$) by using a Perkin-Elmer Fourier transform interferometer (FTIR) at room temperature[11]. The results showed a main absorption peak centered at λ_p = 10.7 μm with a spectral linewidth of $\Delta\nu$ = 500 cm^{-1}.

Figure 3 shows the measured dark current as a function of the bias voltage for InGaAs/InAlAs BTM QWIP at different temperatures. Figure 4 shows the dark current and differential resistance (r_d)versus bias voltage for this QWIP measured at T = 67 K. The asymmetry property of the dark current under positive and negative bias conditions was clearly shown in both figures, which can be attributed to the doping migration effect created during the growth of the quantum well/superlattice layers. The doping impurities in the quantum well spill over to the superlattice barrier layer along the direction of epilayer growth which leads to the asymmetry of the potential barrier on either side of the quantum well. Since the dark current in the BTM QWIP is controlled by the thermionically assisted tunneling current through the miniband, asymmetry in potential barrier on either side of

the quantum well will result in asymmetrical dark current flow under positive and negative bias conditions.

The photocurrent was measured as a function of temperature, bias voltage (V_b), polarization direction, and wavelength using an ORIEL 77250 single grating monochromator and ceramic element infrared source. Figure 5 shows the normalized responsivity versus wavelength measured at V_b = 0, 0.5 V and T = 67 K. As shown in the figure, under the photovoltaic (PV) mode operation (V_b = 0), the detector has a peak response wavelength at λ_p = 10 μm. When a voltage is applied to this QWIP, the photoconductive (PC) mode detection becomes the predominant conduction mechanism for $V_b > 0.5V$. The peak wavelength λ_p for the PC mode detection was found to be at 10.3 μm. A full width at half maximum (FWHM) of $\Delta\nu$ = 232 cm^{-1} ($\sim$ 29 meV) was obtained from Fig.5. The band width $\Delta\lambda/\lambda$ = 24 % from the PC response curve was found to be much narrower than the room-temperature FTIR absorption[11] curve. The intersubband transitions for both the PC and PV modes may be attributed to the resonant transition from the ground state E_{EW1} to the global miniband E_{SL1} states which are aligned with the first excited state E_{EW2} in the quantum well. The intersubband resonant transition (i.e., maximum absorption strength) depends strongly on the location of the first excited state $_{EW2}$ of the quantum well relative to the miniband edge, E_{SL1}[5]. In this BTM QWIP structure, the E_{EW2} lies near the top of the miniband edge E_{SL1}, which results in a strong, narrow-band spectral response in the PV mode detection with a linewidth of $\Delta\lambda$ = 0.7 μm at a half maximum. The bound-to-miniband (BTM) transition QWIP operating in the PV mode offers a unique feature of ultra-narrow bandwidth ($\Delta\lambda/\lambda_p$ = 7 %) infrared detection, which is not attainable in a conventional bound-to continuum transition QWIP. As the bias voltage increases, relative position between the "embedding" localized state E_{EW2} and the"framing" miniband states E_{SL1} can be adjusted by a "controlling bias" due to the different dependence of E_{EW2} and E_{SL1} on the bias voltage. An energy redshift of about 3.6 meV between the resonant states was observed at V_b = 0.5 V and T = 67 K. As expected, a broad-band spectral linewidth of 24 % at V_b = 0.5 V was obtained in the PC mode operation as shown in Fig.5. In the voltage-tunable BTM QWIP structure, not only can the spectral bandwidth be tailored to the desired width (from 7 % to 24 %), but the spectral response peak can also be tuned as well. The photocurrent responsivity R_A and the detectivity D^* for the PC and PV modes were measured at T = 67 K, λ = 10.3 μm and 10 μm, respectively, and the results are shown in Fig. 6. The peak responsivity for the PV mode was found to be 27 mA/W at λ = 10 μm. The photocurrent responsivity R_A, measured at V_b = 0.5, 1.5 V, was found to be 38 mA/W and 145 mA/W, respectively. The detectivity D* was calculated from the measured responsivity and dark current, using the formula $D^*_\lambda = R_A(A\Delta f)^{1/2}/i_n$,

where A is the effective area of the detector, Δf is the noise bandwidth. The dark current shot noise i_n is given by $i_n = \sqrt{4qI_dg\Delta f}$, where g is the optical gain, and may be evaluated from the measured responsivity $R_A = \eta(\lambda/1.24)g$ and the unpolarized quantum efficiency expression $\eta = (1/2)(1\text{-}e^{-2\alpha l})$. Optical gain can also be derived from the noise measurement. The results yielded a peak detectivity $D^*_\lambda = 5.8\times10^9$ cm $\sqrt{Hz}$/W at $\lambda = 10.3$ μm, $V_b = 0.5$ V, and T = 67 K for the PC mode operation. As shown in Fig. 6, the value of D^*_λ decreases with increasing V_b due to the increase of dark current with increasing bias voltage. The zero bias differential resistance r_d was found to be about 450 KΩ at 67 K. Since the detector operating in the PV mode is limited by Johnson noise (i.e., $i_j = \sqrt{4KT/r_d}$), the detectivity D^*_λ for the PV mode was found to be 5.7×10^9 cm $\sqrt{Hz}$/W. In order to verify the zero bias noise, we also measured the noise current by using a lock-in amplifier, which yielded a value of $i_j = 9.0\times10^{-14}$ A/$\sqrt{Hz}$, in good agreement with the calculated value from the Johnson noise expression. Figure 7 shows the measured noise current and differential resistance as a function of the temperature for the QWIP operating at zero bias condition (PV mode), for $40 < T < 65K$. A linear relation was obtained between the semilog plot of noise current (or differential resistance) and temperature. For $V_b < 0.15$ V, the photoresponse at $\lambda_p = 10.3$ μm decreases with increasing bias voltage, indicating that the internal photovoltage is offset by the applied bias voltage in this bias range. For $V_b > 0.15$ V, the photoresponse starts to increase again, which implies that the PC mode conduction becomes dominant when the applied bias exceeds the built-in potential in the QWIP. However, when the polarity of the bias voltage was reversed, the responsivity of the QWIP was found to decrease rapidly and the internal photovoltage disappeared.

To further understand the PV mode detection in the InGaAs/InAlAs BTM QWIP, the short-circuit current (I_{sc}) and open-circuit voltage (V_{oc}) were measured as a function of temperature using a HP4145 at $V_b = 0$, and the results are shown in Fig.8. It is interesting to note that V_{oc} increases monotonically with decreasing temperature for $T \leq 65K$, and I_{sc} increases with decreasing temperature for $T < 77K$ and reaches a saturation value of 0.1 V at T = 45 K. The large V_{oc} observed in this BTM QWIP may be attributed to the doping impurities migration in the direction of growth layers: Part of the doping impurities migrate from doped quantum well to the adjacent superlattice barrier layers. At low temperatures, some electrons from the dopant impurities in the superlattice are trapped in the quantum well due to the lower thermal energy. The separated electrons and positive ionized impurities form a build-in electric field. As temperature decreases, more electrons are trapped in the doped quantum well, which in turn leads to a larger build-in field in the QWIP. For $T > 68K$, electrons are excited out of the quantum well due to increasing

thermal energy and as a result the build-in potential vanishes. The asymmetric distribution of the impurities can be verified by the observed large asymmetrical dark current under positive and negative bias conditions, as can be seen in Figs.3 and 4.

Figure 9 shows the PV mode responsivity R and detectivity D* as a function of temperature measured at $\lambda_p = 10\mu m$ for the BTM QWIP. The responsivity was found to decrease with decreasing temperature, while detectivity increases with decreasing temperature. The measured peak current response was 63 mA/W at $\lambda = 10\mu m$ and T = 65 K. The large responsivity is due to the enhanced absorption in the enlarged quantum well ($110\mathring{A}$) and the smaller electron effective mass m^* ($m^* = 0.042m_o$) [6]. Although the absorption spectral linewidth (full width at half maximum, FWHM) of the transition is equal to 322 $cm^{-1}(\sim 40meV)$, the measured photovoltaic response FWHM ($\sim 68cm^{-1}$) is much narrower than that of the room temperature absorption spectrum and the photoconduction response (FWHM=232 cm^{-1}). Calculation of the transition energy shows that the major transport route of the photovoltaic response is via the excited state of the doped quantum well and the miniband nearby the excited state. For temperature exceeds 67 K, the signal tend to become comparable with noise. This temperature coincides with that of the vanishing V_{oc}, implying that the photovoltaic phenomenon vanishes for $T \geq 67$ K.

The predominant noise current of a BTM QWIP operating in PV mode is due to Johnson noise current $i_J = \sqrt{4kT/r_d}$. From Fig.7, the noise current for the InGaAs BTM QWIP was estimated to be $0.17\ pA/\sqrt{Hz}$, which is about one order of magnitude lower than the photoconductor detectors. From the responsivity and the noise current, the detectivity $D^* = R\sqrt{A}/i_n$ was calculated and the results were shown in Fig.9. As shown in Fig.9, increasing the temperature, D^* will decrease due to the exponential increase in noise current with temperature, whereas the responsivity increases with increasing temperature. The D^* was found to be $7.06 \times 10^9 cm\sqrt{Hz}/W$ at $\lambda_p = 10\mu m$ and T= 65 K, and the dark current was found to be 21 nA. It is noted that D^* was measured using normal incident illumination with metal grating to couple the effective electric field $E_\perp$ into the quantum wells. The coupling quantum efficiency is a strong function of the grating periodicity for a given wavelength. However, the equally spaced square metal grating with a periodicity length of $\Lambda = 10\mu m$ and the width $d = 5\mu m$ of the square metal grating used in this QWIP was not optimized. The geometrical ratio factor $g = d/\Lambda = 0.5$ of the grating yields about 8.3% quantum efficiency [4]. A higher quantum efficiency square metal grating is presented in Section 3.3. The use of this grating can significant increase the value of D^*.

In conclusion, we have demonstrated a new high performance PV and PC dual-mode operation InGaAs/InAlAs QWIP using the voltage-tunable bound-to-miniband (BTM) transition mechanism. Both narrow-band PV mode and broad-band PC mode detections at $\lambda \sim 10$ μm peak wavelength have been achieved. Using the dual-mode operation and bound-to-miniband transition InAlAs/InGaAs QWIP structure grown on InP substrate, it is possible to design high performance two-color staring focal plane arrays and infrared image sensors for use in the 3-5 μm and 8-14 μm wavelength applications. A significant improvement in detectivity and responsivitycan be predicted by using a high quantum efficiency 2-D metal grating coupler on the QWIP.

References

1. J. S. Smith, L. C. Chiu, S. Margalit, A. Yariv, and A. Y. Cho, J. Vac. Sci. Technol. **B1**, 376 (1983).

2. B. F. Levine, K. K. Choi, C. G. Bethea, J. Walker, and R. J. Malik, Appl. Phys. Lett.**50**, 1092 (1987).

3. L. S. Yu and S. S. Li, Appl. Phys. Lett. **59**, 1332 (1991).

4. L. S. Yu, Y. H. Wang, and S. S. Li, Appl. Phys. Lett. **60**, 992 (1992).

5. T. S. Faska, J. W. Little, W. A. Beck, K. J. Ritter, A. C. Goldberg, and R. LeBlanc., Innovative Infrared Photodetector Workshop, JPL, Pasadena, **April** 7-9, 1992.

6. B. F. Levine, G. Hasnain, C. G. Bethea, N. Chand, Appl. Phys. Lett. **54**, 2704 (1989).

7. B. F. Levine, C. G. Bethea, G. Hasnain, V. O. Shen, E. Pelve, R. R. Abbott, and S. J. Hseih, Appl. Phys. Lett. **56**, 851 (1990).

8. H. Asai and Y. Kawamura, Appl. Phys. Lett. **56**, 746 (1990).

9. B. F. Levine, A. Y. Cho, J. Walker , R. J. Malik, D. A. Kleinman, and D. L. Sivco, Appl. Phys. Lett. **52**, 1481 (1988).

10. G. Hasnain, B. F. Levine, D. L. Sivco, and A. Y. Cho, Appl. Phys. Lett. **56**, 770 (1990).

11. L. S. Yu and S. S. Li, Appl. Phys. Lett. **59**, 2712 (1991).

12. M. O. Manasreh, F. Szmulowicz, D. W. Fisher, K. R. Evans, and C. E. Stutz, Appl. Phys. Lett. **57**, 1790 (1990).

13. S. D. Gunapala, B. F. Levine, and N. Chand, J. Appl. Phys. **70**, 305 (1991).

14. A. Raymond, J. L. Robert, and C. Bernard, J. Phys. C **12**, 2289 (1979).

15. K. M. S. V. Bandara, D. D. Coon, and Byungsung O, Appl. Phys. Lett. **53**, 1931 (1988).

16. M. Ramsteiner, J. D. Ralston, P. Koidl, B. Dischler, H. Biebl, J Wagner, and H. Ennen, J. Appl. Phys. **67**, 3900 (1990).

17. A. Kastalsky, T. Duffield, S. J. Allen, and J. Harbison, Appl. Phys. Lett. **52**, 1320 (1988).

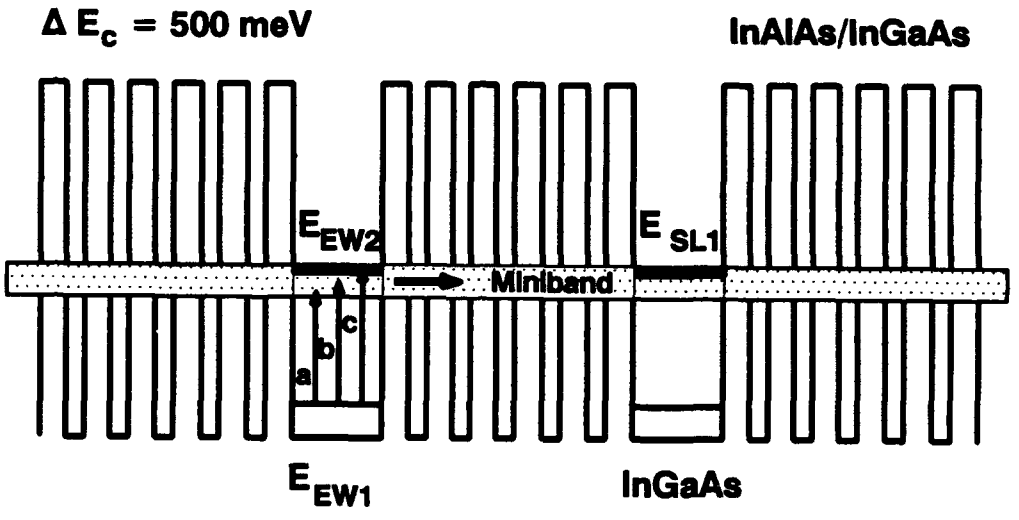

Figure 1. Energy band diagram for an InGaAs/InAlAs BTM QWIP.

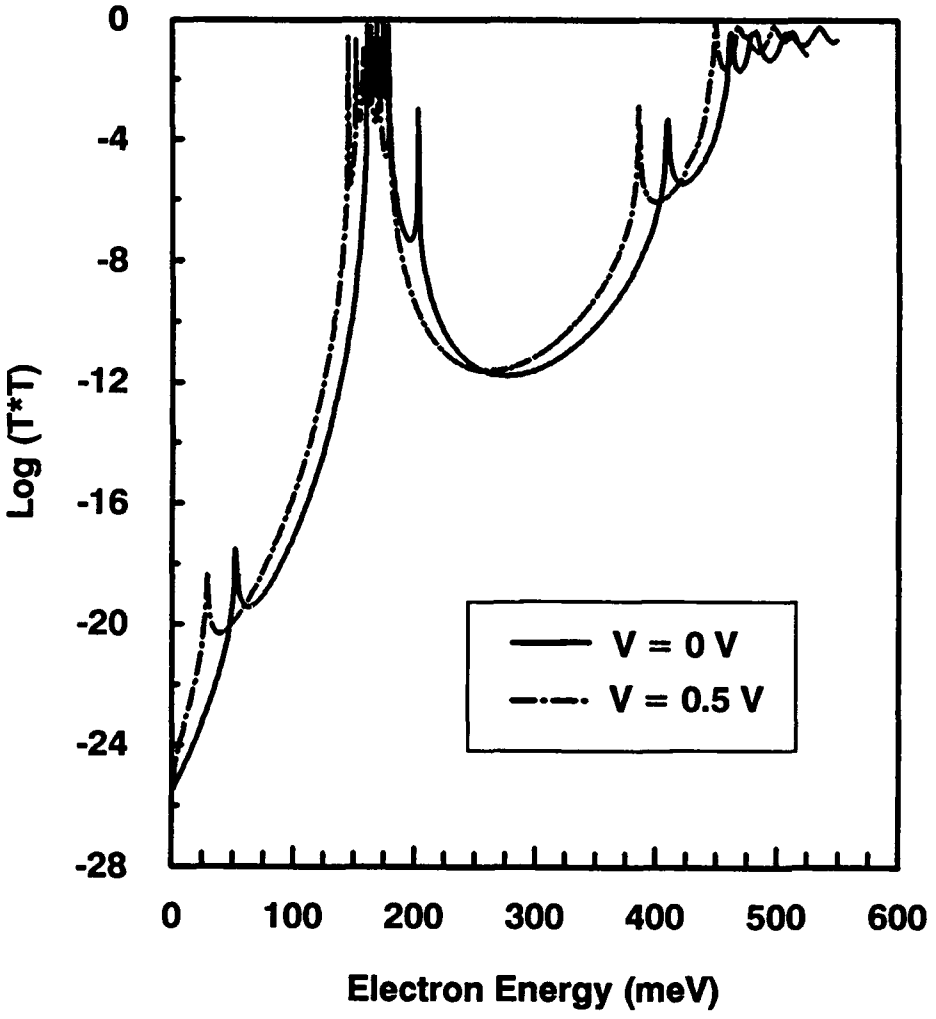

Figure 2. Energy states and transmission probability for an InGaAs/InAlAs BTM QWIP.

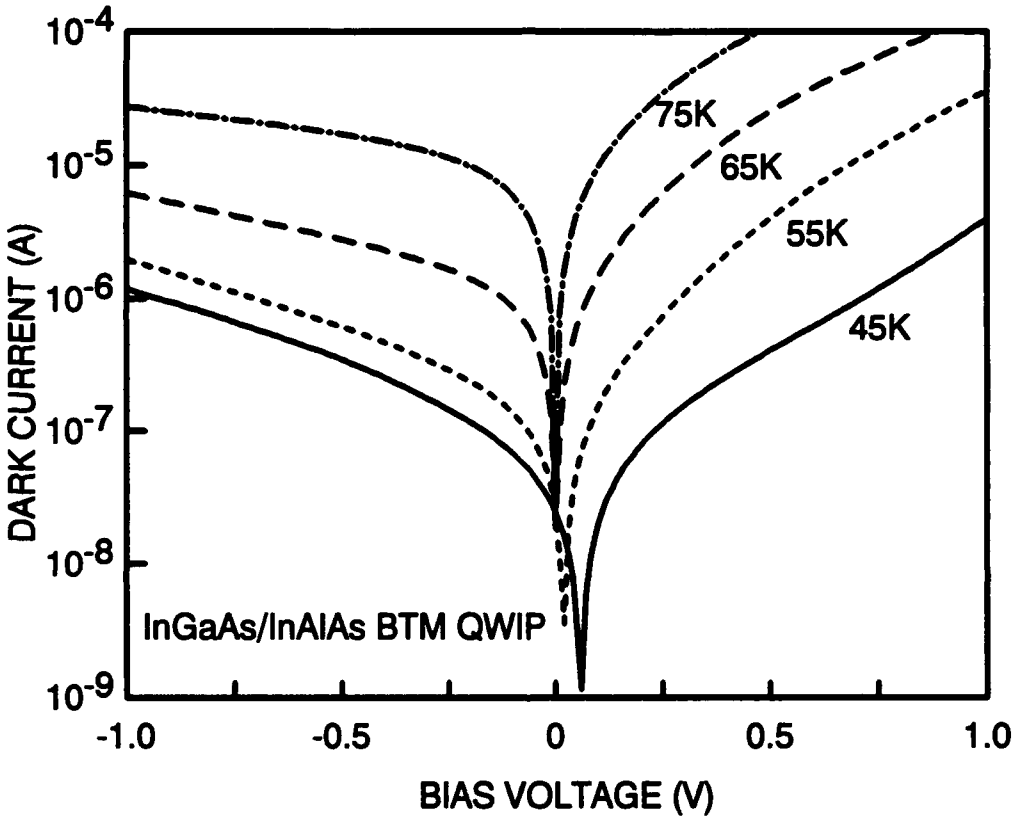

Figure 3 Dark current vs. bias voltage for an InGaAs/InAlAs BTM QWIP for 45 < T < 75 K.

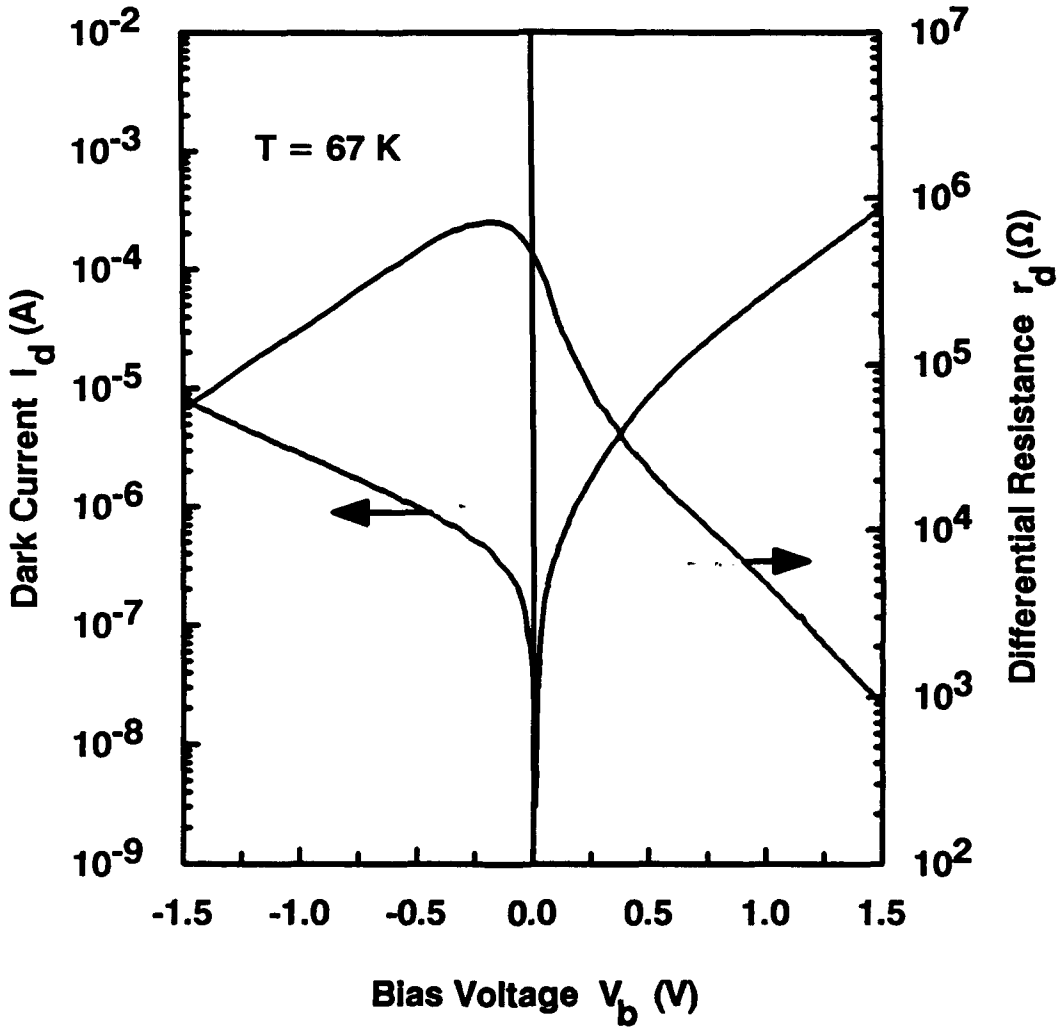

Figure 4 Dark current and differential resistance vs. bias voltage for an InGaAs/InAlAs BTM QWIP at T = 67 K.

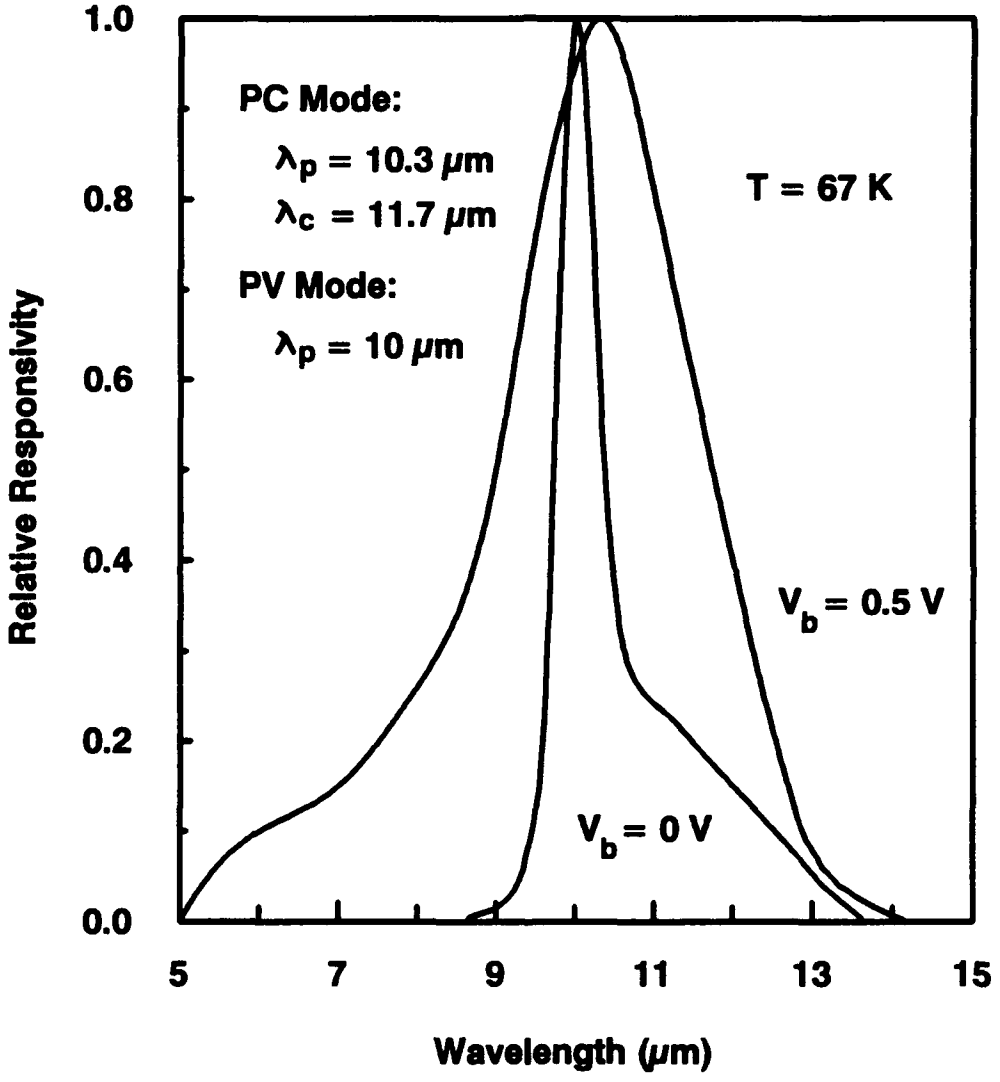

Figure 5 Relative responsivity vs. wavelength for V_b = 0, 0.5V for an InGaAs/InAlAs BTM QWIP at T = 67 K.

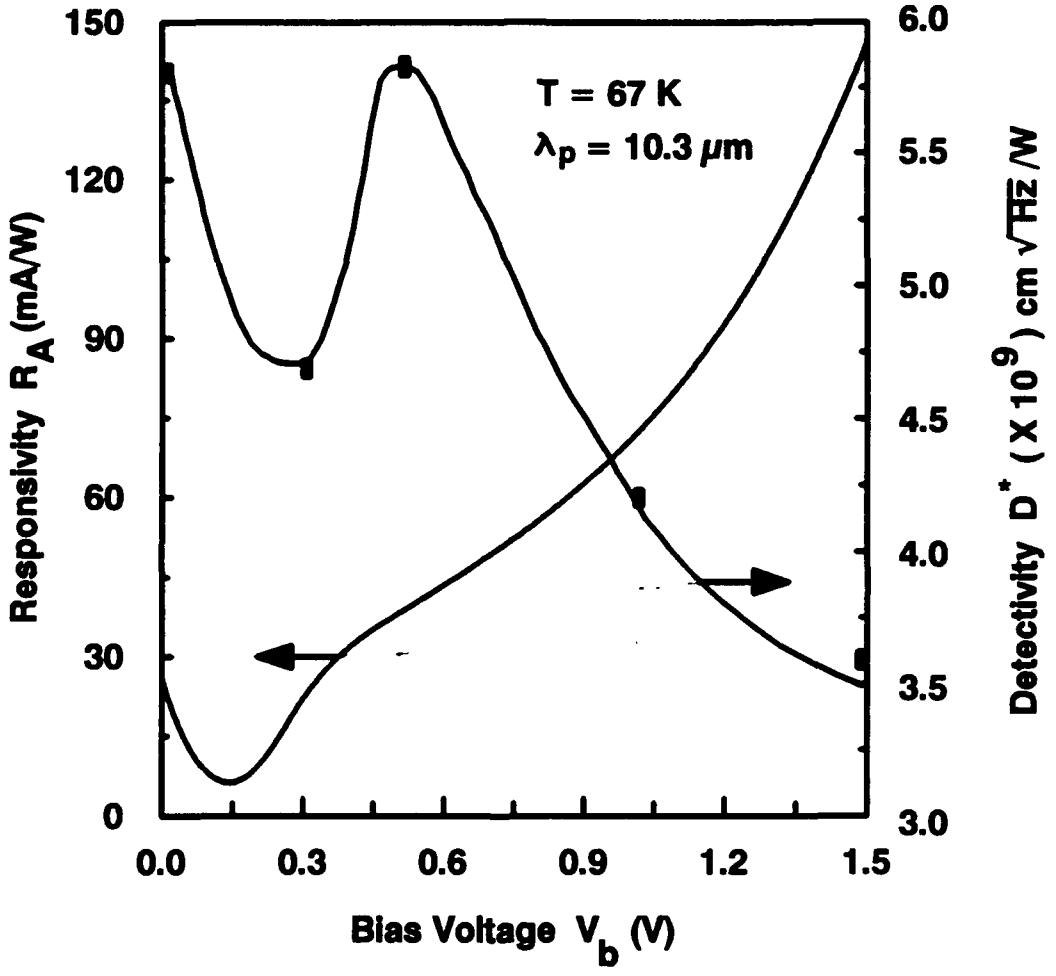

Figure 6 Responsivity and detectivity vs. bias voltage for an InGaAs/InAlAs BTM QWIP .

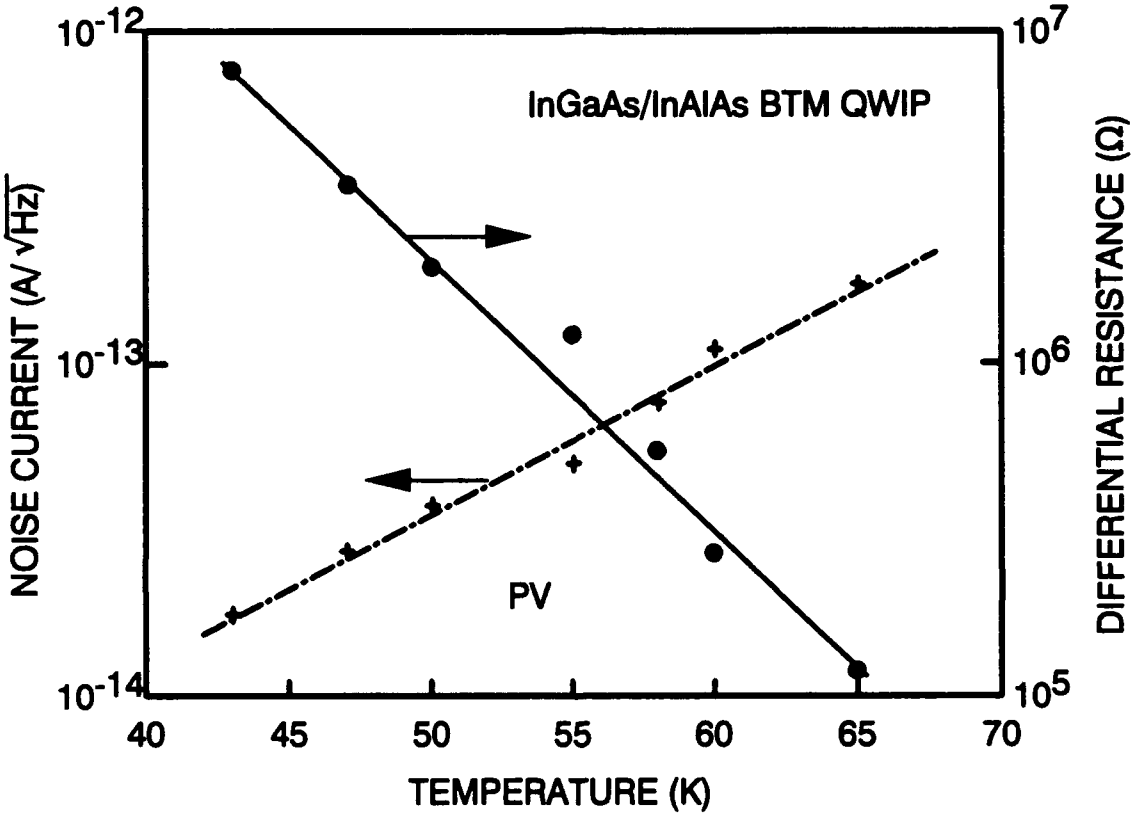

Figure 7 Noise current and differential resistance vs. temperature for an InGaAs/InAlAs BTM QWIP in PV mode detection.

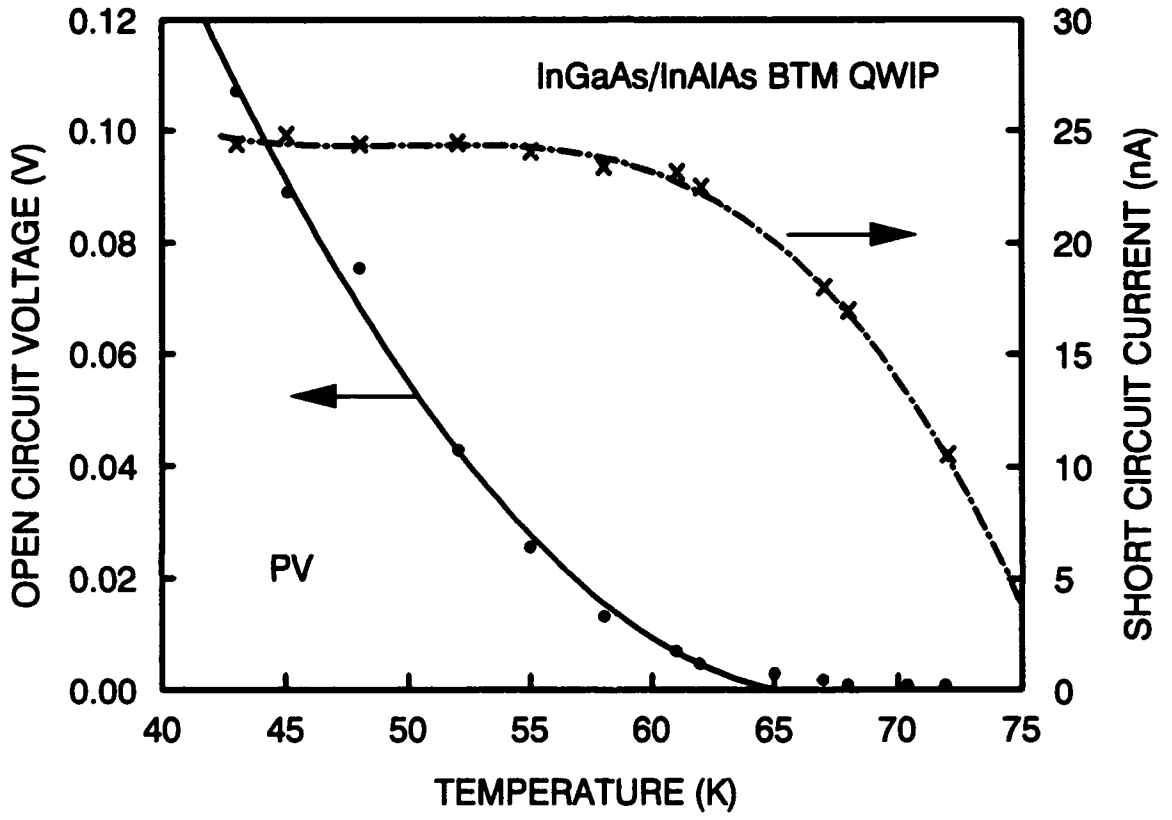

Figure 8 Open-circuit voltage and short-circuit current vs. temperature for an InGaAs/InAlAs BTM QWIP.

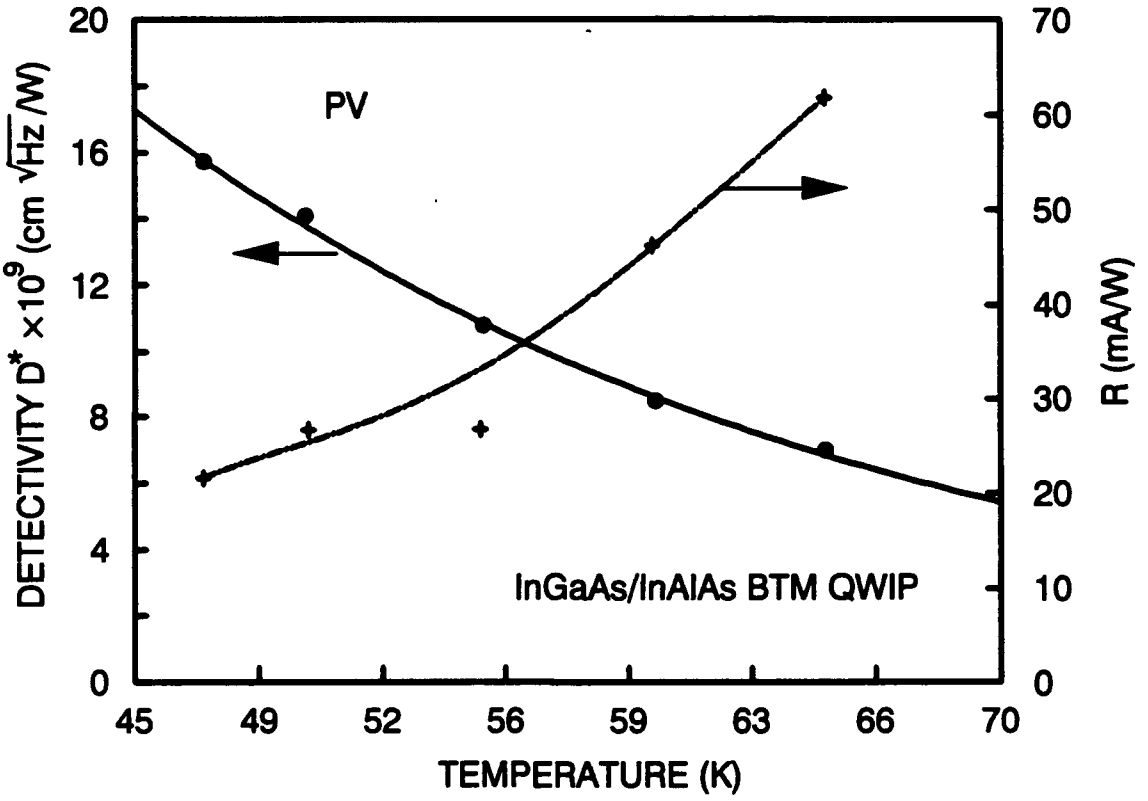

Figure 9 Detectivity and responsivity vs. temperature measured at 10 um wavelength for an InGaAs/InAlAs BTM QWIP.

3.2 Characterization of a normal incidence type-II *AlAs/AlGaAs* QWIP grown on [110] GaAs

Summary: A detailed characterization of the normal incidence type-II AlAs/$Al_{0.5}Ga_{0.5}As$ QWIP grown on [110] GaAs by MBE technique has been carried out. The normal incidence radiation of intersubband transition is achieved in the [110] X-band confined AlAs quantum wells. Two main absorption bands were observed which covers the mid-wavelength infrared (MWIR) of 2 - 8 μm and the long wavelength infrared (LWIR) of 9 -17 μm. The peak photoresponse in the LWIR band occurs at λ =12.5μm with a peak responsivity R = 24 mA/W and a detectivity $D^* = 5 \times 10^9 cm - sqrtHz/W$ at V_b = 2 V and T = 77 K. In the MWIR region, an ultra-high photoconductive gain was observed at λ = 2.2 μm with a responsivity R =110 A/W and a detectivity $D^* = 1.1 \times 10^{12} cm - sqrtHz/W$, at V_b = 6 V and T = 77 K.

3.2.1 Introduction

Many interesting characteristics of intersubband absorption and infrared detection using type-I and type-II quantum well infrared photodetectors (QWIPs) have been investigated extensively in recent years[1-9]. In type-I quantum well structure, the direct bandgap material system is used and hence the shape of constant energy surface is usually spherical. As a result, only the component of infrared (IR) radiation with electric field perpendicular to the quantum well layers will give rise to intersubband transition in the quantum well. This leads to forbidden intersubband transition at normal incidence in type-I QWIPs. In order to achieve strong absorption of normal incidence IR radiation in the quantum wells, indirect bandgap semiconductors are highly desirable for QWIP applications. In the indirect bandgap materials, conduction electrons occupy indirect valleys with ellipsoidal constant energy surfaces. The effective-mass anisotropy (mass tensor) of electrons in the ellipsoidal valleys can provide coupling between the parallel and perpendicular motions of the electrons when the principal axes of one of the ellipsoids are tilted with respect to the growth direction. As a result of the coupling, intersubband transitions at normal incidence in a indirect bandgap QWIP structure are allowed.

Since the AlAs/$Al_{0.5}Ga_{0.5}As$ material systems are indirect bandgap materials, the conduction band minima for the AlAs quantum wells are located at the X point in the Brillouin zone (BZ). The constant energy surface will also undergo change from a typical sphere at the zone center for the direct gap material (i.e. GaAs) to off-center ellipsoids of an indirect gap material (i.e. AlAs). For AlAs, there are six ellipsoids along [100] axes with the centers of the ellipsoids located at about

three-fourth of the distance from the BZ center. By choosing a proper growth direction such as [110], [111], [113], [115] directions[7,8], due to the anisotropic band structure, it is possible to realize large area normal incidence IR radiation in a type-II AlAs/AlGaAs QWIP.

Recently we demonstrated for the first time a normal incidence type-II QWIP using an indirect gap $AlAs/Al_{0.5}Ga_{0.5}As$ system[7,9] grown on [110] GaAs substrate. We use the indirect bandgap $AlAs$ for the quantum well layer and $Al_{0.5}Ga_{0.5}As$ as the barrier layer. Since the compound of $Al_xGa_{1-x}As$ becomes an indirect bandgap material for $x > 0.45$, the conduction-band minimum shifts from the Γ-band to the X-band. The conduction band offset of $Al_{0.5}Ga_{0.5}As$ over the $AlAs$ is about 180 meV. Figure 1 shows a schematic conduction-band diagram for the type-II indirect $AlAs/Al_{0.5}Ga_{0.5}As$ quantum well structure, in which the electrons are confined inside the $AlAs$ layer. The intersubband transition is between the ground bound state in the AlAs quantum well and the first excited state in the well or the quasi-continuum states above the $AlAs/Al_{0.5}Ga_{0.5}As$ barrier layers.

3.2.2 Theory and Experiment

The indirect gap AlAs/AlGaAs QWIP structure was grown on a [110] GaAs substrate by using the molecular beam epitaxy (MBE) technique. A 1.0 μm thick n-GaAs buffer layer with $N_d = 2\times10^{18}\ cm^{-3}$ was first grown on the [110] oriented semi-insulating GaAs substrate, followed by the growth of 20 periods of $AlAs$ quantum wells with a well width of 30 Å and doping concentration of $2 \times 10^{18}\ cm^{-3}$. The barrier layers on either side of the quantum well consist of an undoped $Al_{0.5}Ga_{0.5}As$ (500 Å) barrier layer. Finally, a 0.3 μm thick n^+-GaAs cap layer with a dopant density of $2 \times 10^{18}\ cm^{-3}$ was grown on top of the quantum well layers for ohmic contacts.

To derive the basic equations for the normal induced intersubband transitions and the corresponding indirect type-II quantum well infrared photodetectors, we start with the Hamiltonian description of quantum mechanics for an electron[10]

$$H_o = \frac{p^2}{2m} + V(\mathbf{r}) + \frac{\hbar}{4m^2c^2}\sigma \cdot (\nabla V(\mathbf{r}) \times \mathbf{p}), \tag{1}$$

where m, p, and σ are the mass, momentum, and spin operators on an electron, respectively. $V(\mathbf{r})$ is a periodic potential function. The system under consideration consists of an assembly of electrons and the infrared radiation field. The Hamiltonian of this system, H, may be written as the sum of the unperturbed Hamiltonian H_0 and the perturbing Hamiltonian H_{rad}' which represents the

interaction between the electrons and the incident infrared photon written as[11]

$$H'_{rad} = -\frac{q}{mc}\mathbf{A}\cdot[\mathbf{P} + (\frac{\hbar}{4mc^2})\sigma \times \nabla V], \tag{2}$$

where $\mathbf{A}$ is the vector potential of the IR radiation field and $\mathbf{P}$ is the canonical momentum.

The matrix element of intersubband transition in the quantum well is given by[12,13]

$$M_{fi} = \int \phi_{kf} H'_{rad} \phi_{ki} d\mathbf{r} = -q(\frac{2\pi}{Vcn\hbar\omega})^{1/2} \mathbf{e}_\omega \cdot \nabla_{\mathbf{k}} \mathcal{E}_{\mathbf{k}} \tag{3}$$

where the parameters i and f denote the initial and final states, $\mathbf{e}_\omega$ is the unit polarization vector of the incident photon, ω the light frequency, q the electronic charge, V the volume of the crystal, n the refractive index, and $\mathcal{E}_{||}$ is conduction band energy of the X-valley material in the well.

It can be shown that the intersubband transition probability $\eta_{\mathbf{k}}$ may be expressed as[12,14]

$$\begin{aligned}\eta_{\mathbf{k}} &= \frac{2\pi}{\hbar}|M_{fi}|^2 \delta(E_f - E_i - \hbar\omega) \\ &= \frac{B_0 k_z^2}{\omega}\left[\frac{\partial^2 \mathcal{E}_{\mathbf{k}}}{\partial k_z \partial k_x}(\mathbf{e}_\omega \cdot \mathbf{x}_0) + \frac{\partial^2 \mathcal{E}_{\mathbf{k}}}{\partial k_z \partial k_y}(\mathbf{e}_\omega \cdot \mathbf{y}_0) + \frac{\partial^2 \mathcal{E}_{\mathbf{k}}}{\partial k_z \partial k_z}(\mathbf{e}_\omega \cdot \mathbf{z}_0)\right]^2 \delta(E_f - E_i - \hbar\omega)\end{aligned} \tag{4}$$

where B_0 is a constant equal to $\frac{q^2\pi^2}{cVn\hbar^2}$; $\mathbf{x}_0$, $\mathbf{y}_0$, and $\mathbf{z}_0$ are the directional unit vectors.

For an indirect type-II AlAs quantum well layers grown along [110] direction of GaAs substrate, due to the tilted anisotropic energy band with minimum point away from the center, the second partial derivatives $\frac{\partial^2 \mathcal{E}_{\mathbf{k}}}{\partial k_z \partial k_i}$ (i = x, y) can be different from zero. Therefore, it is possible to excite long wavelength intersubband transitions in the quantum well under normal incidence IR radiation. However, for a direct type-I system (e.g., GaAs) due to the isotropic spherical energy surface and the axis symmetrical parabolic band $E = E_z + \hbar^2(k_y^2 + k_z^2)/2m^*$, it always has $\frac{\partial^2 \mathcal{E}_{\mathbf{k}}}{\partial k_z \partial k_i} = 0$, (where $i \neq z$). The corresponding transition probability becomes

$$\eta_k = \frac{B_0 k_z^2}{\omega}\left[\frac{\partial^2 \mathcal{E}_{\mathbf{k}}}{\partial k_z \partial k_z}(\mathbf{e}_\omega \cdot \mathbf{z}_0)\right]^2 \delta(E_f - E_i - \hbar\omega) \tag{5}$$

Equation (5) reveals that the optical transition would become zero for the type-I structures under normal incidence radiation.

3.2.3 Results and Discussion

A BOMEM interferometer was used to measure the infrared absorbance of the AlAs/AlGaAs QWIP sample. In order to eliminate substrate absorption, we performed absorbance measurements

on the QWIP sample with and without the quantum well layers. The absorbance data were taken using normal incidence radiation at 77 K and room temperature. The absorption coefficients deduced from the absorbance data are shown in Fig. 2. Two absorption peaks at λ = 6.8 μm and 14 μm were detected, while two additional absorption peaks at 2.3 μm and 3.5 μm were also observed. All the absorption coefficients measured at 77 K were found to be about a factor of 1.2 higher than the room temperature values. From our theoretical analysis, the 14 μm peak with absorption coefficient of about 2000 cm^{-1} is the transition between the ground state and the first excited state in the quantum well, while the 6.8 μm peak with absorption coefficient of about 1600 cm^{-1} is due to transition between the ground state and the continuum states. The absorption strengths at 2.3 μm and 3.5 μm are very strong, with a narrower linewidth than that of the 14 μm peak. The exact physical origins of these absorption peaks are not clear, and require further study.

To facilitate the normal incidence infrared illumination, an array of QWIPs with a 210 $\times$ 210 μm^2 mesa structure were chemically etched down to n^+-GaAs buffer contact layer on the GaAs substrate. Finally, AuGe/Ni/Au ohmic contact was formed on top of the QWIP structures, leaving a central sensing area of 190 $\times$ 190 μm^2 for normal incidence illumination. Device characterization was performed in a liquid-helium cryogenic dewer. A HP4145 semiconductor parameter analyzer was used to measure the dark current versus bias voltage.. Figure 3 shows the measured dark current as a function of the bias voltage for temperatures between 68 and 89 K. Substantial reduction in device dark current was achieved in the present type-II structure. The photocurrent was measured using a CVI Laser Digikrom 240 monochromator and an ORIEL ceramic element infrared source. A pyroelectric detector was used to calibrate the radiation intensity from the source. Figure 4 shows the LWIR photoresponse and absorption coefficient for wavelengths from 9 to 18 μm. The peak response wavelength is at λ_p =12.5 μm with a cutoff wavelength of 14.5 μm and a peak responsivity of R_p = 24 mA/W at T = 77 K and V_b = 2 V. A broader linewidth of $\Delta\lambda/\lambda$ = 30% than the type-I QWIP and a 1.5 μm shorter wavelength shift was found in this peak wavelength at λ_p =12.5 μm. Detectivity was found to be about 1.1 $\times 10^9$ cm $(Hz)^{1/2}/W$ under above condition.

Figure 5 shows the photovoltaic (PV) spectral response bands in the visible to mid-IR wavelengths.The main response band covers a relatively narrow band width from λ = 2 μm to 3.25 μm, with $\Delta\lambda/\lambda$ = 15.9 %. The peak response occured at λ_p = 2.2 μm with a responsivity R = 32 mA/W at T = 77 K. The responsivity for this detector remains nearly constant for $V_b \leq$ 2 V. However, for $V_b >$ 2 V, an exponential increase in the responsivity with the applied bias voltage was observed, as is shown in Fig. 6. A huge photoconductivity gain of 3,200 (as compared to the value at V_b = 0)

was obtained at $V_b = 6$ V. Although the exact mechanism for this large photocurrent gain is not clear, possible explanations are given as follows. In the type-II indirect AlAs/AlGaAs QWIP, free carriers are confined in the AlAs quantum well formed in the X-conduction band minima, which has a larger electron effective mass than that in the Γ-band valley. When a resonant radiation impinges on this QWIP, electrons in the ground-state of the X-valley quantum well are excited resonantly to the excited states in the Γ-band of AlAs well. Due to the effective mass difference between the X-band and the Γ-band, electron velocity and mobility in the Γ-valley will be much higher compared to the electrons in the X-band valley. Since the photocurrent is proportional to the electron velocity and the mobility (i.e., $I_{ph} = Aqv_d g\tau$, where A is the effective area of the detector, v_d is the drift velocity, g is the photogeneration rate, $1/\tau$ is the recombination rate of electrons in the Γ-band), a large increase in the photocurrent is expected when bias induced transition from the X-band to Γ-band takes place under illumination. Since this process is the inverse of negative differential resistance (NDR), a super differential resistance (SDR) can be expected from the X-band to the Γ-band transition, which is highly desirable for the MWIR and LWIR QWIP applications. The photoresponse at $\lambda = 3.5$ and 6.8 μm were not measured due to light source and monochromator limitation and will be performed in the near future.

In conclusion, we have demonstrated the multispectral responses in normal incidence type-II AlAs/AlGaAs QWIPs using an indirect X-band $AlAs/Al_{0.5}Ga_{0.5}As$ system. The desirable normal incidence radiation is allowed due to the tilted and anisotropic energy band structure grown on a [110] GaAs substrate. The detector was found to have two peak wavelength responses: one at $\lambda_p = 2.2$ and the other at 12.5 μm, and spectral response ranges from 2 to 3.25 and 9 to 18 μm, respectively. The capabilities of normal incidence, large spectral sensing range, and low device dark current make the present type-II AlAs/AlGaAs QWIPs highly desirable for many infrared applications. Further studies on the interaction effects between the X- and Γ-bands, transition coupling, bandgap engineering, and hot electron transport mechanisms in the type II indirect III-V multiquantum well structures may lead to new and improved infrared detectors, lasers, and modulators.

References

1. P. Dawson, B. A. Wilson, C. W. Tu, and R. C. Miller, Appl. Phys. Lett. **48**, 541 (1986).

2. B. F. Levine, R. J. Malik, J. Walker, K. K. Choi, C. G. Bethea, D. A. Kleinman, and J. M. Vandenberg, Appl. Phys. Lett., 50, 273 (1987).

3. K. K. Choi, B. F. Levine, C. G. Bethea, J. Walker, and R. J. Malik, Appl. Phys. Lett., 50, 1814; 52 1979 (1988).

4. E. R. Brown and S. J. Eglash, Phys. Rev. **41**, 7559 (1990).

5. P. Lefebvre, B. Gil, H. Mathieu, and R. Planel, Phys. Rev.**39**, 5550 (1989).

6. M. Dabbicco, R. Cingolani, M. Ferrara, K. Ploog, and A. Fisher, Appl. Phys. Lett.**59**, 1497 (1991).

7. L. S. Yu, S. S. Li, and P. Ho, Electron. Lett. **28**, 1468 (1992).

8. J. Katz, Y. Zhang, and W. I. Wang, Appl. Phys. Lett., Oct., (1992).

9. P. Ho, P. A. Martin, L. S. Yu, Y. H. Wang, and S. S. Li, accepted, J. Vacuum Science Technology, Oct. (1992).

10. E. O. Kane, J. Phys. Chem. Solid **1**, 249 (1957).

11. L. I. Schiff, Quantum Mechanics McGraw-Hill, New York, (1968).

12. E. Haga and H. Kimura, J. Phys. Soc. Jpn. **18**, 777 (1963).

13. F. Stern and W. E. Howard, Phys. Rev. **163**, 816 (1967).

14. C. L. Yang, D. S. Pan, and R. Somoano, J. Appl. Phys. **65**, 3253 (1989).

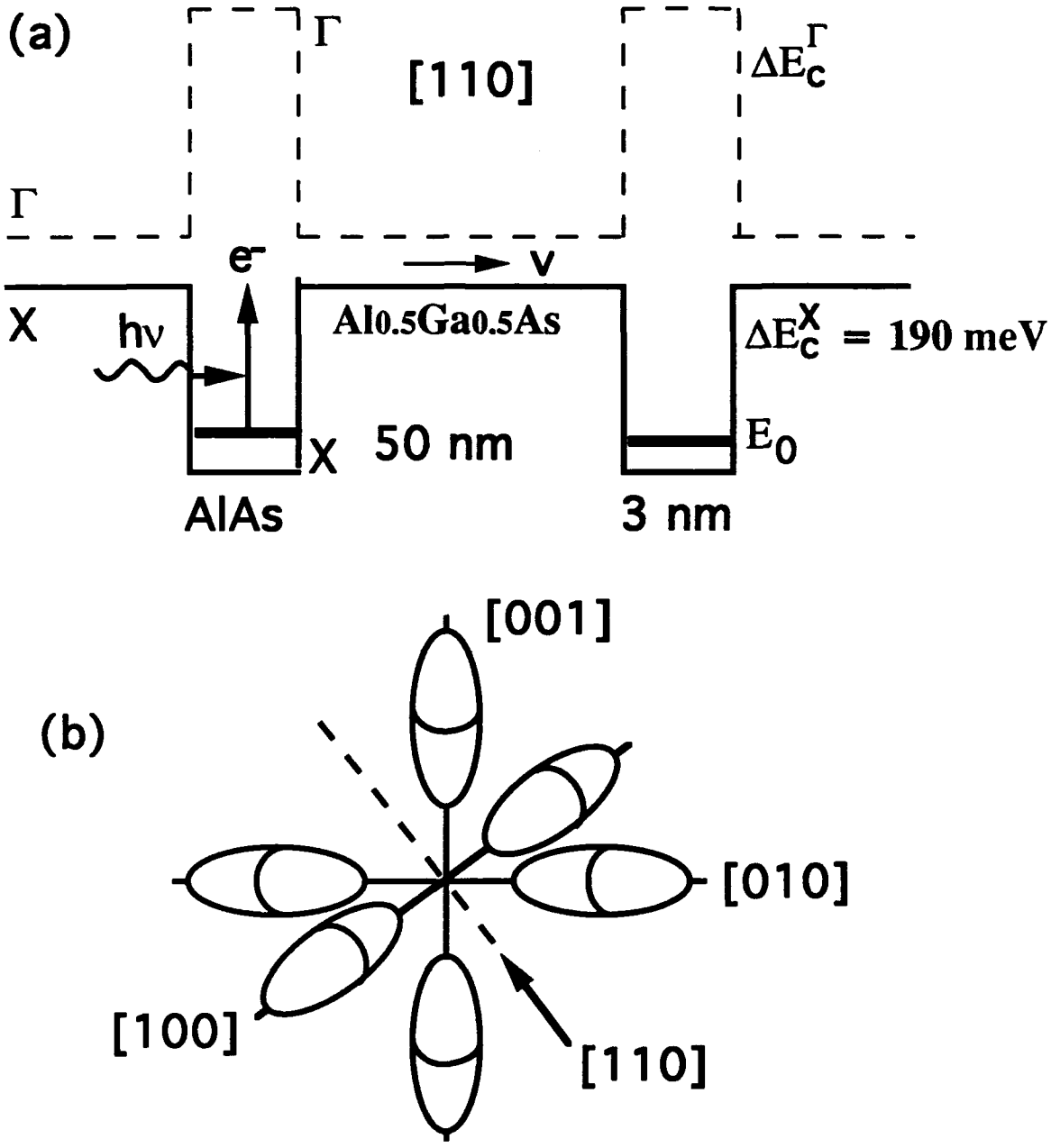

Figure 1 The conduction band diagram for the normal incidence type-II AlAs/Al0.5Ga0.5As QWIP. Solid line is for the X-band and dashed line denotes the Γ-band.

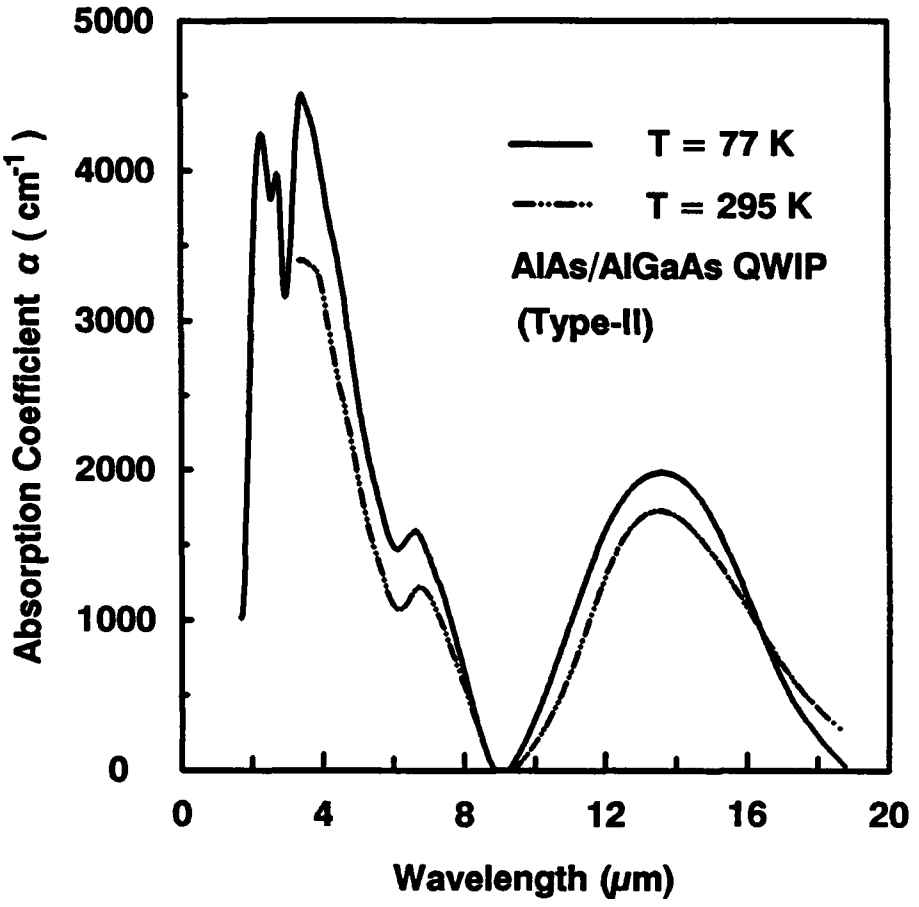

Figure 2 Intersubband absorbance versus wavelength by BOMEM interferometer at normal incidence for the type-II QWIP measured at 77 K and room temperature.

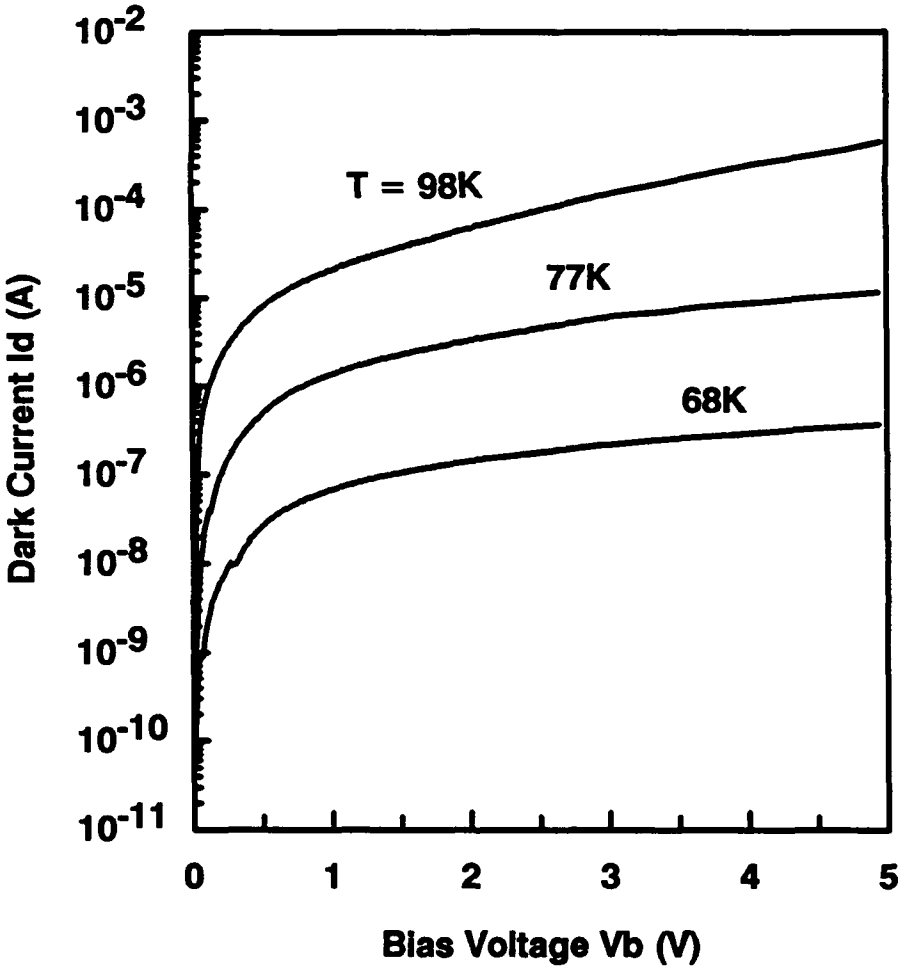

Figure 3 Dark current versus applied bias voltage for T = 68, 77, 89 K.

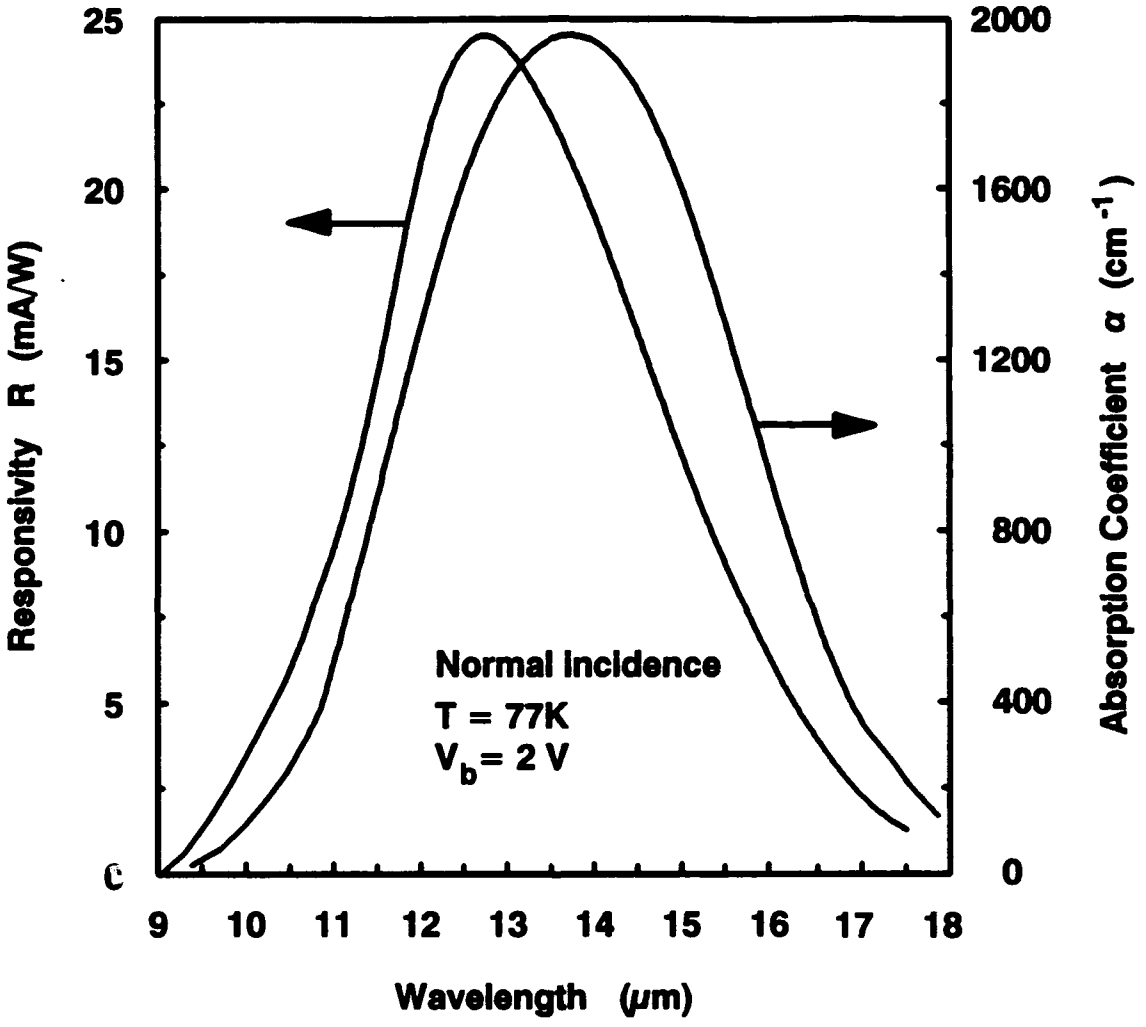

Figure 4 Responsivity and absorption coefficient versus wavelength at $V_b = 2$ V, T = 77 K, and for $9 < \lambda < 18$ μm.

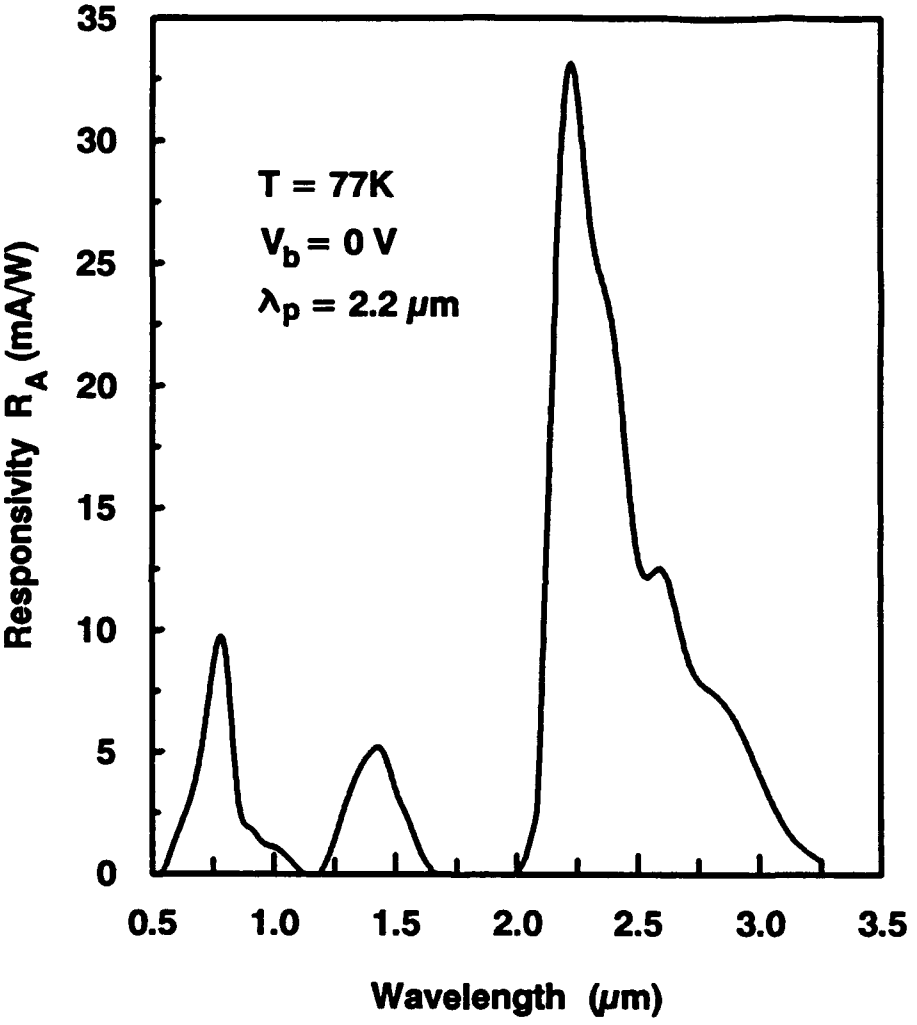

Figure 5 Photovoltaic responsivity versus wavelength for the type-II AlAs/AlGaAs QWIP measured at $V_b = 0$, T = 77 K, and for $0.5 < \lambda < 3.3$ μm.

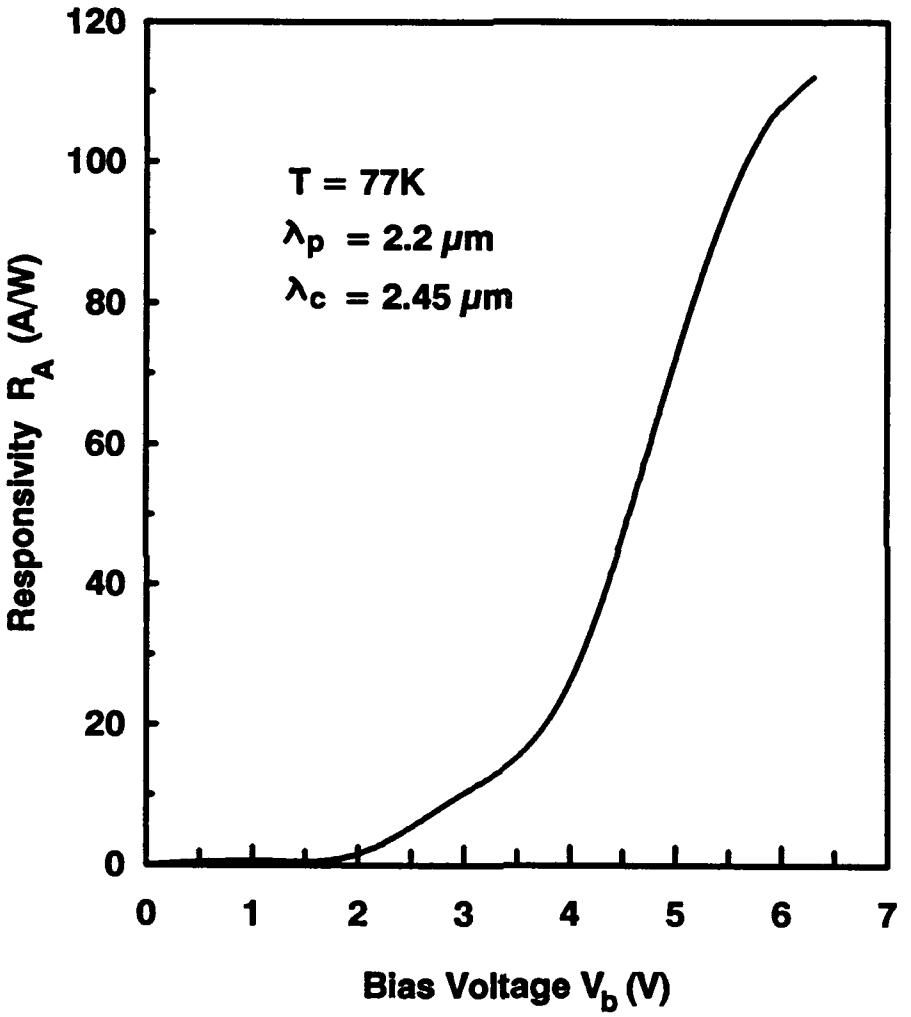

Figure 6 Responsivity versus bias voltage for the type-II QWIP shown in Fig.5 at a peak response wavelength $\lambda = 2.2$ μm and T = 77 K.

3.3 Design of 2-D Square Metal Grating Couplers for a GaAs BTM QWIP

Summary: A numerical simulation of 2-D (two-dimensional) transmission square mesh metal grating and reflection square cross metal grating coupled structures formed on top of a miniband transport (BTM) GaAs/AlGaAs quantum well infrared photodetector (QWIP) has been carried out. The main advantage of these grating structures is that the coupling of normal incident infrared radiation into the doped quantum wells of a BTM QWIP is independent of its polarization direction. Two normalized parameters (i.e., $s = \lambda/g$ and $h = a/g$, where g is the grating period and a is width of the square mesh or cross grating) are introduced to characterize the 2-D metal grating structures. Using the universal charts plotting from the normalized parameters, the total power and angle of the first order transmitted or refracted light are determined for different grating periods and sizes in the 6 to 14 μm wavelength range. Moreover, the absorption constant and coupling quantum efficiency for the BTM QWIP are also be calculated from these results.

3.3.1 Introduction

Recently, there has been a considerable interest in the long wavelength intersubband quantum well infrared photodetectors (QWIPs) for operating in the 8μm to 12 μm atmospheric window region at $77K$[1-15]. Most of the QWIPs reported in the literature are fabricated using a larger bandgap III-V semiconductor material system such as GaAs/AlGaAs instead of the more difficult narrow bandgap material such as HgCdTe. The GaAs QWIP offers a very promising approach for the low background, long wavelength infrared detection due to the matured GaAs growth and processing technology. Thus, low cost and extremely uniform large area focal plane arrays (FPAs) can be fabricated using GaAs QWIPs for staring IR image sensor applications. However, the intersubband transition QWIPs using GaAs/AlGaAs material system do not absorb normal incident IR radiation on the surface of QWIP, since the electric field vector of incident light must be polarized perpendicular to the quantum well in order to induce intersubband transitions[16-18]. As a result, the angle of incidence with respect to the QW layers must be different from zero in order to induce intersubband absorption in the quantum well. However, for FPAs applications, a response in normal incident light is required. This may be solved by incorporating a lamellar grating[2,7,10], which has a low coupling efficiency due to its polarization sensitivity. A double periodic metal grating formed on the top of a QWIP can be employed to deflect the normal incident light into an absorbable angle independent of light polarization. There are two approaches to form a double periodic grating on the QWIP: one approach is to deposit a metal grating directly onto the

detectors as shown in Fig.1 and Fig. 8, and another appraoch is to etch the top surface layer of the QWIP followed by metal deposition[3]. The former has the advantages over the latter in that it uses a simple and planar metal grating structure which can avoid the unwanted nonuniform etching on the detector surface and hence reduces the processing difficulties. In this section we report a numerical analysis of a 2-D transmission square mesh and reflection square cross metal grating formed directly on the top cap layer of the GaAs BTM QWIP.

Let us consider the electromagnetic (EM) waves impinging on a QWIP under normal incidence illumination. The radiation scattered by the metal grating consists of the transverse electric (TE) polarization with the electric field parallel to the QW planes and the TM polarization with one component of the electric field perpendicular to the planes. Only TM components of the incident IR radiation leads to intersubband absorption in the quantum well. In the transmission square mesh metal grating structure shown in Fig.1, for a unit amplitude normal incident light, the total power of each order refracted mode depends on the 'normalized wavelength' $s = \lambda/g$ (where g is the grating period and λ is the wavelength) and the 'strip factor' $h = a/g$ (where a is the width of the square aperture in the metal mesh). Furthermore, the angle between higher order transmitted wave and grating normal is determined soly by the parameter s. Thus, the intersubband absorption in the quantum well of a BTM QWIP is determined by the total power of the higher order transmitted TM waves and the refracted angle. The purpose of this work is to produce universal plots from which the power of higher order transmitted TM waves and the refracted angle can be determined for different sizes and grating period of 2-D square aperture mesh grating couplers formed on a GaAs BTM QWIP. Together with the absorption constant of intersubband transition, these plots provide a convenient overview of the mesh metal grating characteristics and of the various design possibilities for the BTM QWIPs.

3.3.2 Basic Theory

The basic theory used in deriving the unknown scattered waves for the transmission square mesh metal grating coupler in a BTM QWIP is based on the modal expansion technique [20]. The mesh metal grating consists of an infinitesimal perfect conducting screen perforated with square apertures distributed periodically along two orthogonal coordinates $\vec{x}$ and $\vec{y}$ as shown in Fig. 1. In this figure we employed spherical coordinates, θ is the angle between the wave propagation vector $\vec{k}$ and the normal to the plane of the grating, and ϕ is the angle between the x- axis and the projection of $\vec{k}$ on the x-y plane. The mesh metal grating is formed on top of the QWIP. The

distribution of the electromagnetic waves near the grating array is in the form of Floquet mode functions according to wave theory in a periodic structure. For this reason, under normal incidence radiation condition the solution of scalar time independent wave equation is given by

$$\psi_{pq} = e^{-ju_p x} \cdot e^{-jv_q y} \cdot e^{-jw_{pq} z} \tag{6}$$

where the wave vectors u_p, v_q, and w_{pq} are given respectively by

$$u_p = \frac{2\pi p}{g} = k \cdot \sin\theta \cdot \cos\phi \tag{7}$$

$$v_q = \frac{2\pi q}{g} = k \cdot \sin\theta \cdot \sin\phi \tag{8}$$

$$w_{pq} = \begin{cases} \sqrt{k^2 - t_{pq}^2} & \text{for } k^2 \geq t_{pq}^2 \\ -j\sqrt{t_{pq}^2 - k^2} & \text{for } k^2 \leq t_{pq}^2 \end{cases}$$

where p,q=0,$\pm$1,$\pm$2,...,$\pm\infty$

and

$$t_{pq}^2 = u_p^2 + v_q^2$$

The vector orthonormal mode functions for the TE and TM modes transverse with respect to $\hat{z}$ can be expressed as

$$\vec{\Phi}_{pq}^{TE} = \frac{1}{g}\left(\frac{v_q}{t_{pq}}\hat{x} - \frac{u_p}{t_{pq}}\hat{y}\right)\psi_{pq} \qquad \text{for TE modes}$$

$$\vec{\Phi}_{pq}^{TM} = \frac{1}{g}\left(\frac{u_p}{t_{pq}}\hat{x} + \frac{v_q}{t_{pq}}\hat{y}\right)\psi_{pq} \qquad \text{for TM modes} \tag{9}$$

The wave admittances looking into the air in $+\hat{z}$ direction are

$$\xi_{pq}^{TE} = \frac{w_{pq}}{k}\frac{1}{Z_0}$$

$$\xi_{pq}^{TM} = \frac{k}{w_{pq}}\frac{1}{Z_0} \tag{10}$$

where $Z_0 = \sqrt{\frac{\mu_0}{\epsilon_0}}$ is the free space characteristic impedance. Assuming that the impedance between all the quantum well layers are perfectly matched and the intersubband absorption is complete, no waves will be reflected from the other end of the QWIP. Under this condition, the modal admittances for TE and TM waves looking into the QW region from $z = 0^+$ plane are to replace Z_0 in Eq.(5) by $Z_d = \sqrt{\frac{\mu_0}{\epsilon_0 \epsilon_s}}$ of GaAs as following

$$\xi_{pq}^{dTE} = \frac{w_{pq}}{k}\frac{1}{Z_d}$$

$$\xi_{pq}^{d^{TM}} = \frac{k}{w_{pq}} \frac{1}{Z_d} \tag{11}$$

A plane wave with unit electric field intensity normal incidence in the ϕ plane can be expressed as the sum of TE and TM plane waves, i.e.,

$$\vec{E}^i = \sum_{r=1}^{2} A_{00r} \vec{\Phi}_{00r} \tag{12}$$

where A_{00r} is the magnitude of the incident field component which depends on the polarization direction. The third subscript $r = 1$ or 2 is used to designate the TE and TM Floquet modes respectively. Similarly, the reflected waves and transmitted waves can also be expressed in terms of the Floquet modes with reflection coefficients R_{pqr} and transmission coefficients B_{pqr} as follows:

$$\begin{aligned} \vec{E}^t &= \sum_{r=1}^{2} A_{00r} \vec{\Phi}_{00r} + \sum_{p} \sum_{q} \sum_{r=1}^{2} R_{pqr} \vec{\Phi}_{pqr} \\ &= \sum_{p} \sum_{q} \sum_{r=1}^{2} B_{pqr} \vec{\Phi}_{pqr} \end{aligned} \tag{13}$$

where Eq.(8) includes the boundary condition that the tangential electric field in the aperture is continuous. The orthonormal waveguide modes $\vec{\Psi}_{mnl}$ span the space of the aperture itself other than the Floquet modes $\vec{\Phi}_{pqr}$ were used to expand the unknown electric field distribution in the aperture in order to satisfy the boundary condition, which has been shown to provide a faster convergence.

$$\vec{E}^t = \sum_{m} \sum_{n} \sum_{l=1}^{2} F_{mnl} \vec{\Psi}_{mnl} \tag{14}$$

where the unknowns F_{mnl} are the coefficients given in the waveguide modes expression. Finally, a matrix equation can be obtained as

$$\left[Y_{MNL}^{mnl}\right] [F_{mnl}] = [I_{mnl}] \tag{15}$$

where

$$\begin{aligned} Y_{MNL}^{mnl} &= \sum_{p} \sum_{q} \sum_{r=1}^{2} (\xi_{pqr} + \xi_{pqr}^{d}) C_{pqr}^{MNL*} C_{pqr}^{mnl} \\ C_{pqr}^{mnl} &= \int \int_{aperture} \vec{\Phi}_{pqr}^{*} \cdot \vec{\Psi}_{mnl} da \end{aligned} \tag{16}$$

and

$$I_{mnl} = \sum_{r=1}^{2} A_{00r} \xi_{00r} C_{00r}^{mnl*} \tag{17}$$

is the input matrix. The higher order transmission coefficients are given by

$$B_{pqr} = \sum_{m} \sum_{n} \sum_{l=1}^{2} F_{mnl} C_{pqr}^{mnl} \qquad p, q \neq 0, 0 \tag{18}$$

Since $F_{mnl} \propto \lambda$ and $C_{pqr}^{mnl} \propto 1/\lambda$ for a given g, the transmission coefficient B_{pqr} is a function of λ/g. The angle between the electric field of the higher order transmitted TM Floquet mode $B_{pq2}\vec{\Phi}_{pq2}$ and the $\hat{z}$ direction is designated as γ_{pq2}, and cosine of this angle depends on the order of transmitted waves and normalized wavelength $s = \lambda/g$ as given by

$$\cos\gamma_{pq2} = \frac{\lambda}{g} \cdot \sqrt{p^2 + q^2} \tag{19}$$

The 2-D grating coupled GaAs/AlGaAs BTM QWIP structure used in the present analysis is based on the bound ground state in the enlarged well to the global miniband in the superlattice which has been reported by Yu and Li[4], as shown in Fig. 2. Only in the miniband the electrons are freely to move in the perpendicular direction to the QW layers and may give rise to an electric signal. The intersubband absorption constant can be expressed[12] by

$$\alpha = \left(\frac{e^2\hbar^3}{m^{*2}n_r\epsilon_0 c}\right) \cdot \frac{n_e \cos^2\gamma}{\hbar\omega} \cdot \frac{T^2\sqrt{(E - E_{min})(E_{max} - E)}}{(U + S_1)^2 - S_1(E_{max} - E)} \tag{20}$$

where e is the electronic charge, m^* is the effective mass, n_r is the refractive index of the medium, c is the speed of light, n_e is the electron density in the wells, ω is the angular frequency of the EM waves, γ is the angle between the electric vector of the incident IR radiation and the motion vector of electrons, E_{max} and E_{min} are the two extreme edge of the miniband as shown in Fig. 2. All other parameters, T, U, and S_1 in Eq.(14) depend on the specific quantum well structure. Substituting Eq.(14) into (15), we can readily calculate the absorption constant in the spectral range of interest.

3.3.3. Results and Discussion

The evanescent modes excited by the square mesh metal grating produce no photoresponse in the quantum well intersubband transition[11], neither do the TE modes. Therefore, the following discussion will focus on the propagating TM modes in the transmitted region (i.e., the side where the QW is located). It is convenient to use the two normalized parameters '$s = g/\lambda$' and the strip factor $h = a/g$ to illustrate the universal plots for the transmission square mesh metal grating coupled BTM QWIP.

Rigarous calculations were made by using fourty waveguide modes, the addition of more modes made no significant change in the transmission coefficients. When analyzing meshs with larger strip factor ($a/g > 0.85$), a much larger number of waveguide modes were required to simulate the wave distribution at the metal edge. Large strip factor is undesirable for the practical QWIP, since it is more difficult to fabricate grating coupler with periodicity and aperture size less than 2 μm. Let us

now consider the case of a normal incident unit amplitude electromagnetic wave impinging on the square mesh metal grating at zero degree angle with respect to the grating normal. The effective coupling is due to nonzero order transmitted TM Floquet modes, since the TE Floquet modes have an angle $\gamma = 90°$ in Eq.(15). Figure 3 shows the first universal plot, which illustrates the normalized total power of the first order TM transmitted wave $B_{012}\vec{\Phi}_{012}$, $B_{0-12}\vec{\Phi}_{0-12}$, $B_{-102}\vec{\Phi}_{-102}$ and $B_{102}\vec{\Phi}_{102}$ varies with the normalized wavelength $s = \lambda/g$ for different $h = a/g$. In this figure, we modified the transmitted power by a factor $\frac{2*3.25^2}{1+3.25^2}$ to eliminate the refiection effect owing to the impedance mismatch between air ($n_r = 1$) and GaAs (n_r=3.25 at 77 K). The first order transmitted waves emerge when the wavelength of IR radiation in GaAs is smaller than the grating period, that is, $s = \lambda/g < 3.25$. For the same reason, within the spectral range in Fig. 3, only one far field reflected waves $R_{001}\vec{\Phi_{001}}$ in the free space was found, and all other higher order refracted waves were eliminated. This is due to the fact that free space wavelength λ is greater than the grating period g and thus makes the grating coupler operating in the non-refraction region. Next, the square mesh metal grating is indistinguishable in both x and y directions. The total normalized power of the first order transmitted wave generated by x and y components of the incident wave remains the same for different input polarizations. In other words, the grating is independent of polarization. A relatively flat curve for $h = a/g = 0.5$ as shown in Fig. 3 may be treated as a better choice for coupling the IR radiation more effectively into the QWIP. Figure 4 illustrates the normalized total power of the second order TM transmitted components $B_{\pm 112}\vec{\Phi}_{\pm 112}$ and $B_{1\pm 12}\vec{\Phi}_{1\pm 12}$ as a function of the normalized wavelength s for various values of h. A comparison of Figs. 3 and 4 reveals that the larger the first order transmission modes the larger the power of the second order transmitted modes is. The second order transmitted wave emerges for $s < \frac{3.25}{\sqrt{2}}$ with total power about 50 % smaller than that of the first order transmitteded modes.

Figure 5 shows a universal plot that relates $\cos\gamma_{pq2}$ to the normalized wavelength of the higher order transmitted waves, where γ is the angle between the electric field vector and the grating normal. The relationship for the first order transmitted waves (i.e. $|p| + |q| = 1$ in the notation of Floquet modes $\vec{\Phi}_{pqr}$) is given by

$$\cos\gamma_{pq2} = \frac{\lambda}{g} \tag{21}$$

The relationship for the second order transmitteded waves with $|p| = |q| = 1$ is :

$$\cos\gamma_{pq2} = \frac{\lambda}{g} \cdot \sqrt{2} \tag{22}$$

We next calculate absorption constant on $\cos^2\gamma_{pq2}$ versus wavelength in a 2-D square mesh grating coupled GaAs BTM QWIP. The mesh grating period is selected in the region where s falls between 0.7 and 1 for the first order refracted waves. In this case $\cos^2\gamma$ is greater than 1/2, which corresponds to the 45° launching. If we select the curve with $h = 0.5$ in Fig. 3 by multipling the grating period $g = 4\mu$m to the coordinate, a rather flat coupling curve over a broad wavelength range from 9 to 12 μm appears, as shown in Fig. 6. By substituting the corresponding $\cos\gamma$ in Fig. 5 and using the QWIP parameters given in Fig. 2 in Eq.(15), we obtained the absorption constant versus wavelength for the GaAs BTM QWIP as shown in Fig.7 (a). The aperture width of the mesh grating in the above design example was found to be $a = (4\mu\text{m})\cdot 0.5 = 2\ \mu$m. From Fig. 7(a), the quantum efficiency[12] η can be determined by using the expression

$$\eta = (\mathcal{P}_{eff}) \cdot (1 - e^{-\alpha l}) \tag{23}$$

where $\mathcal{P}_{eff}$ is the effective coupling power of the light and l is the total length of the doped quantum wells. In the present case, $l = (88\mathring{A}) \cdot (40\textit{periods}) = 3520\mathring{A}$ and η is shown in Fig. 7(b).

Similarly, the characteristic curves of the first order TM refraction waves for a reflection square cross metal grating coupler shown in Fig. 8 may be plotted in Fig.9. The basic equations for design such a metal grating coupler are described in Appendix. A strong coupling region located in the 8.5 to 11.5 μm wavelength range as shown in Fig. 9 is available for coupling the reflection mode normal incident IR radiation into the QWIP. The absorption constant spectrum of the square cross metal reflection grating is the same as that of square mesh metal grating, as illustrated in Fig. 7(a). Figure 10 shows a comparison of the quantum efficiency for the GaAs BTM QWIP shown in Fig. 2 coupled by the 2-D square mesh and cross metal grating couplers. Basically, they have the same coupling characteristics in the 9 to 12 μm wavelength range and are both polarization independent. A minor drawback exists for the square mesh metal grating coupler in that a sharp dip of the first order refracted wave coupling power occurs at about 9.2μm as shown in Fig.6, which corresponds to the normalized wavelength $s = \frac{1}{\sqrt{2}}$ of medium refractive index $n_r = 3.25$ for GaAs at $77K$.

In conclusion, we have performed a detailed numerical analysis of a GaAs BTM QWIP covered with two different types of 2-D square metal gratings. It is shown that for a given QWIP the total power and the refracted angle of the higher order TM transmitted waves depend on two normalized parameters, $s = \lambda/g$ and $h = a/g$, which are functions of wavelength and grating dimensions. By using the universal plots shown in Figs.3 and 5, the optimum grating period and grating width can be determined for any specified IR spectrum. In addition, the absorption constant and quantum efficiency for a 2-D metal grating coupled QWIP can be calculated from these universal plots.

APPENDIX

The refracted EM waves in the reflection square cross metal grating coupler were derived by using the ***method of moment*** technique[11,21]. The grating consists of arrays of perfect conducting plates with infinitesimal thickness compared to the wavelength. The square conducting plate arrays are arranged periodically along the two orthogonal coordinates $\vec{x}$ and $\vec{y}$ as shown in Fig. 8. In this figure, θ is the angle between the wave propagation vector $\vec{k}$ and the normal to the plane of the grating, and ϕ is the angle between the x axis and the projection of $\vec{k}$ on the x-y plane. The distribution of electromagnetic field near the array is in the form of Floquet mode functions according to wave theory in a periodic structure. For normal incidence the solution of scalar time independent wave equation is given by

$$\psi_{pq} = e^{-ju_p x} \cdot e^{-jv_q y} \cdot e^{-jw_{pq} z} \tag{24}$$

where the wave vectors u_p, v_q, and w_{pq} are given respectively by

$$u_p = \frac{2\pi p}{g} = k \cdot \sin\theta \cdot \cos\phi \tag{25}$$

$$v_q = \frac{2\pi q}{g} = k \cdot \sin\theta \cdot \sin\phi \tag{26}$$

$$w_{pq} = \begin{cases} \sqrt{k^2 - t_{pq}^2} & \text{for } k^2 \geq t_{pq}^2 \\ -j\sqrt{t_{pq}^2 - k^2} & \text{for } k^2 \leq t_{pq}^2 \end{cases}$$

where p,q=0,$\pm$1,$\pm$2,...,$\pm\infty$

and

$$t_{pq}^2 = u_p^2 + v_q^2$$

The orthonormal mode functions for the TE and TM modes transverse with respect to $\hat{z}$ can be expressed as

$$\vec{\Phi}_{pq}^{TE} = \frac{1}{g}\left(\frac{v_q}{t_{pq}}\hat{x} - \frac{u_p}{t_{pq}}\hat{y}\right)\psi_{pq} \qquad \text{for TE modes}$$

$$\vec{\Phi}_{pq}^{TM} = \frac{1}{g}\left(\frac{u_p}{t_{pq}}\hat{x} + \frac{v_q}{t_{pq}}\hat{y}\right)\psi_{pq} \qquad \text{for TM modes} \tag{27}$$

The wave impedances in the $\hat{z}$ direction are

$$\eta_{pq}^{TE} = \frac{k}{w_{pq}} Z_0$$

$$\eta_{pq}^{TM} = \frac{w_{pq}}{k} Z_0 \tag{28}$$

where $Z_0 = \sqrt{\frac{\mu_0}{\epsilon_0 \epsilon_s}}$ is the characteristic impedance. A plane wave with unit electric field intensity normal incidence in the ϕ plane can be expressed as the sum of TE and TM plane waves, that is

$$\vec{E}^i = \sum_{r=1}^{2} A_{00r} \vec{\Phi}_{00r} \tag{29}$$

where A_{00r} is the magnitude of incident field component which depends on the polarization direction. The third subscript $r = 1$ or 2 is used to designate the TE and TM Floquet modes, respectively . Similarly, the scattered field can also be expressed in terms of the Floquet modes and reflection coefficients R_{pqr} as follows

$$\vec{E}^s = \sum_{p} \sum_{q} \sum_{r=1}^{2} R_{pqr} \vec{\Phi}_{pqr} \tag{30}$$

The boundary condition is that the electric field in the conducting plate equals zero

$$\vec{E}^i + \vec{E}^s = 0 \qquad \text{over the plate (at } z = 0) \tag{31}$$

It has been shown that the current modes $\vec{\Psi}_{mnl}$ other than the Floquet modes $\vec{\Phi}_{pqr}$ were used to expand the induced current $-\hat{z} \times \vec{H}^s$ in the conducting plate in order to provide a faster convergence[16], which are the dual field functions of the transverse electric field function of the aperture spanned by the conducting plate. Finally, an equation in the following matrix expression can be obtained

$$\left[Z_{MNL}^{mnl}\right] [B_{mnl}] = [D_{mnl}] \tag{32}$$

where the unknown B_{mnl} are the coefficients given in the current expression with

$$Z_{MNL}^{mnl} = \sum_{p} \sum_{q} \sum_{r=1}^{2} \eta_{pqr} C_{pqr}^{MNL*} C_{pqr}^{mnl}$$

$$C_{pqr}^{mnl} = \int \int_{plate} \vec{\Phi}_{pqr}^{*} \cdot \vec{\Psi}_{mnl} da \tag{33}$$

and

$$D_{mnl} = \sum_{r=1}^{2} A_{00r} C_{00r}^{mnl*} \tag{34}$$

is the input matrix. The reflection coefficients are

$$R_{pqr} = -\eta_{pqr} \sum_{m} \sum_{n} \sum_{l=1}^{2} B_{mnl} C_{pqr}^{mnl} \tag{35}$$

Due to the dependence of $B_{mnl} \propto \lambda$ and $C_{pqr}^{mnl} \propto 1/\lambda$ for a given g, the reflection coefficients R_{pqr} are a function of λ/g. The angle between the electric field of the higher order TM refracted mode $R_{pq2}\vec{\Phi}_{pq2}$ and the $\hat{z}$ direction is designated as γ_{pq2}, and cosine of this angle depends on the order of refracted waves and normalized wavelength $s = \lambda/g$ as given by

$$\cos\gamma_{pq2} = \frac{\lambda}{g} \cdot \sqrt{p^2 + q^2} \tag{36}$$

References

1. K. W. Goossen and S. A. Lyon, Appl. Phys. Lett. **47**, 1257 (1985).
2. J. Y. Andersson, L. Lundqvist, and Z. F. Paska, Appl. Phys. Lett. **58**, 2264 (1991).
3. J. Y. Andersson, L. Lundqvist, and Z. F. Paska, Appl. Phys. Lett. **59**, 857 (1991).
4. L. S. Yu and S. S. Li, Appl. Phys. Lett. **59**, 1332 (1991).
5. L. S. Yu and S. S. Li, and P. Ho, Appl. Phys. Lett. **60**, 992 (1992).
6. B. F. Levine, C. G. Bethea, V. O. Shen, and R. J. Malik, Appl. Phys. Lett. **57**, 383(1990).
7. R. J. Baüerle, T. Elsaesser, and W. Kaiser, Phys. Rev. B **38**, 4307(1988).
8. K. M. S. V. Bandara. D. D. Coon, and Byungsung O, Appl. Phys. Lett. **53**, 1931 (1988).
9. C. G. Bethea, B. F. Levine, et. al., IEEE Trans. **ED-38**, 1118 (1991).
10. G. Hasnian, B. F. Levin, C. G. Bethea, R. A. Logan, J. Walker, and R. J. Malik, Appl. Phys. Lett. **54**, 2515 (1989).
11. K. W. Goossen and S. A. Lyon, Appl. Phys. Lett.**53**, 1027 (1988).
12. D. D. Coon, R. P. G. Karunasiri, and L. Z. Liu, Appl. Phys. Lett. **47**, 289 (1985).
13. B. F. Levine, R. J. Malik, J. Walker, K. K. Choi, C. G. Bethea, D. A. Kleinman, and J. M. Vandenberg, Appl. Phys. Lett. **50**, 273 (1987)
14. B. F. Levine, C. G. Bethea, G. Hasnian, V. O. Shen, E. Pelve, and P. R.Abbott, Appl. Phys. Lett. **56** 851 (1990).

15. S. G. Gunapala, B. F. Levine, D. Ritter, R. Hamm, and M. B. Panish, Appl. Phys. Lett. **58**, 2024 (1991).

16. F. Stern, Phys. Rev. Lett. **33**, 960 (1974).

17. S. J. Allen, Jr., D. C. Tsui, and B. Vinter, Solid State Commun. **20**, 425 (1976).

18. L. C. West and S. J. Eglash, Appl. Phys. Lett. **46**, 1156 (1985).

19. B. F. Levine, K. K. Choi, C. G. Bethea, J. Walker, and R. J. Malik, Appl. Phys. Lett. **50**, 1092 (1987).

20. C. C. Chen, IEEE Trans. **MTT-18**, 627 (1970).

21. C. C. Chen, IEEE Trans. **AP-18**, 660 (1970).

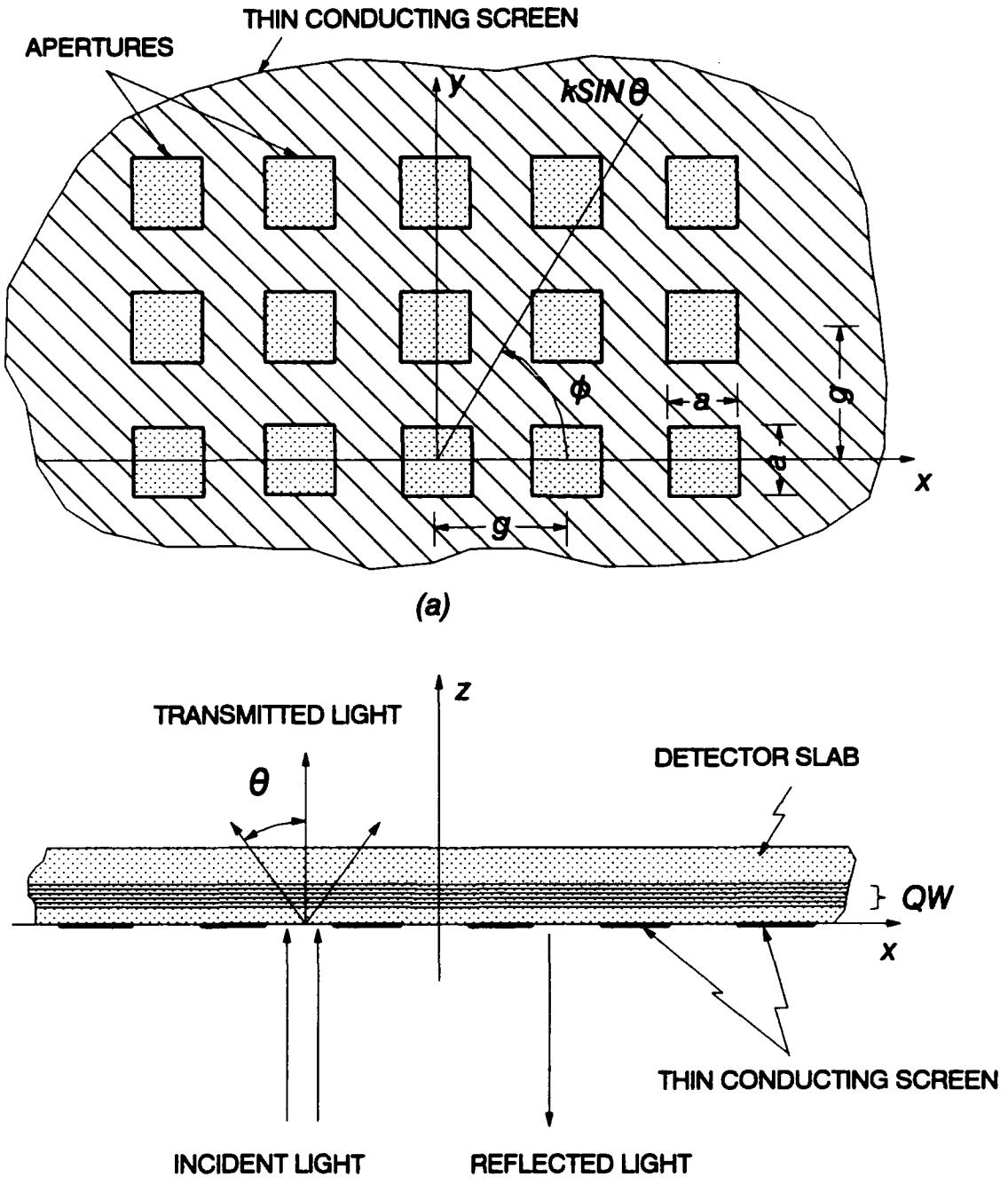

Figure 1 Schematic diagram showing the square mesh metal grating and the directions of incident and scattered waves. (a) Top view, and (b) side view.

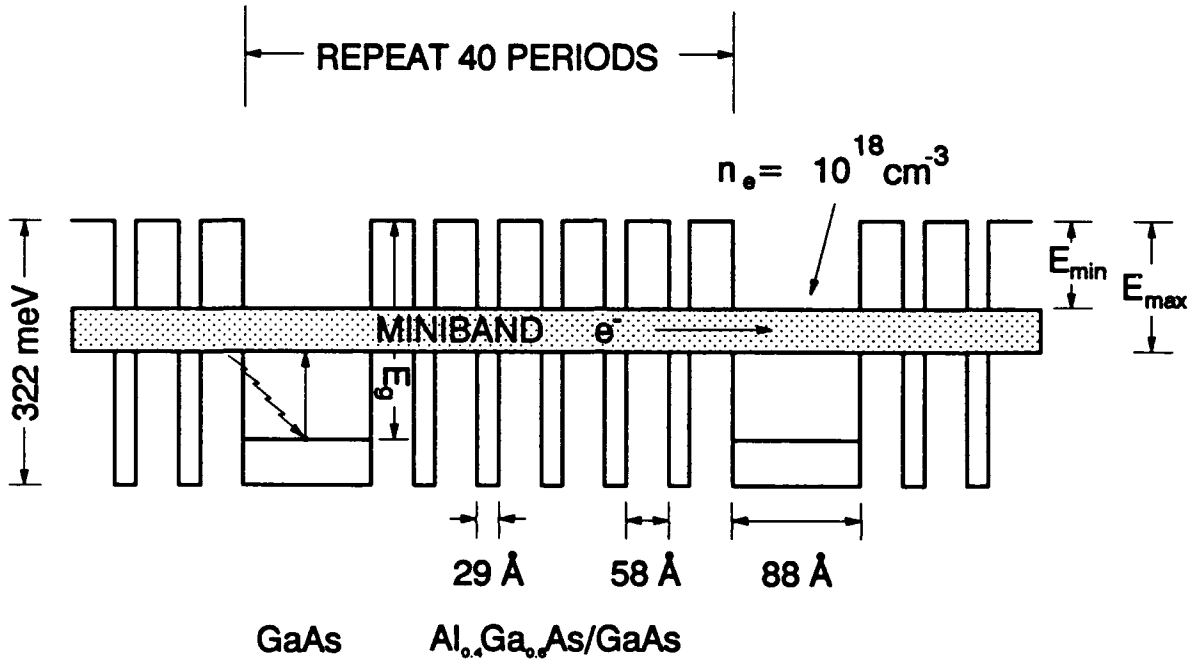

Figure 2 The energy band diagram for a bound-to-miniband (BTM) transition GaAs/AlGaAs quantum well infrared photodetector (QWIP).

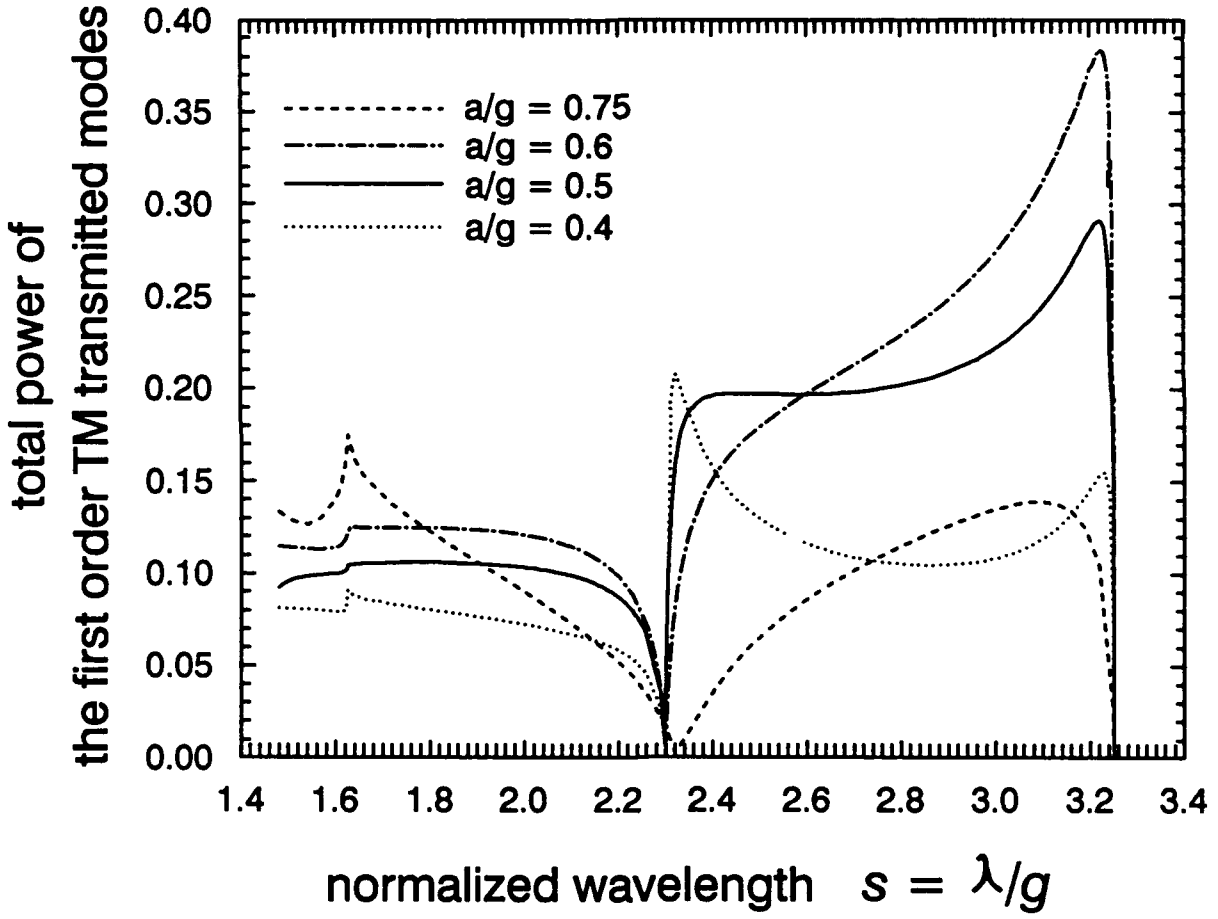

Figure 3 Normalized power of the first order transmitted waves versus normalized wavelength $s = \lambda/g$ for different values of $h = a/g$, where a is the size of square mesh metal grating and g is the grating period.

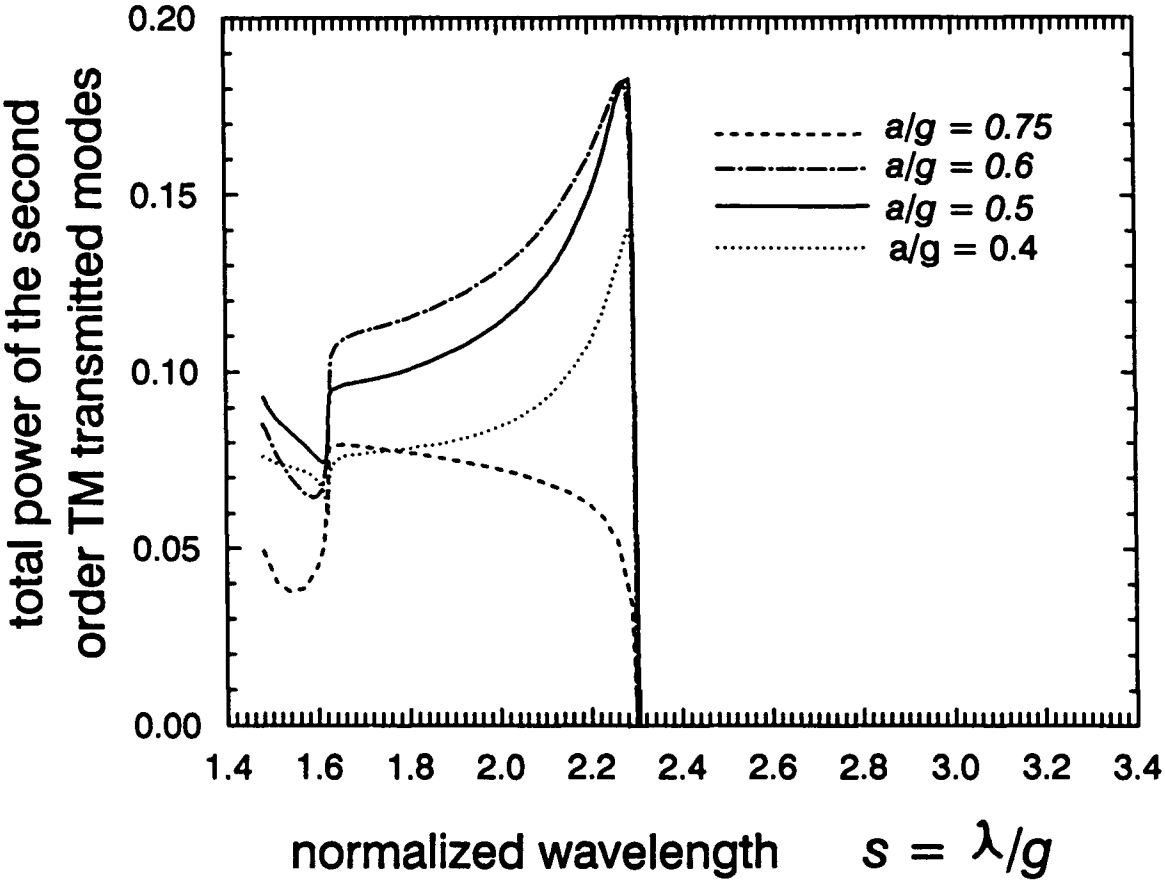

Figure 4 Normalized power of the second order transmitted waves as a function of $s = \lambda/g$ for different values of h=a/g.

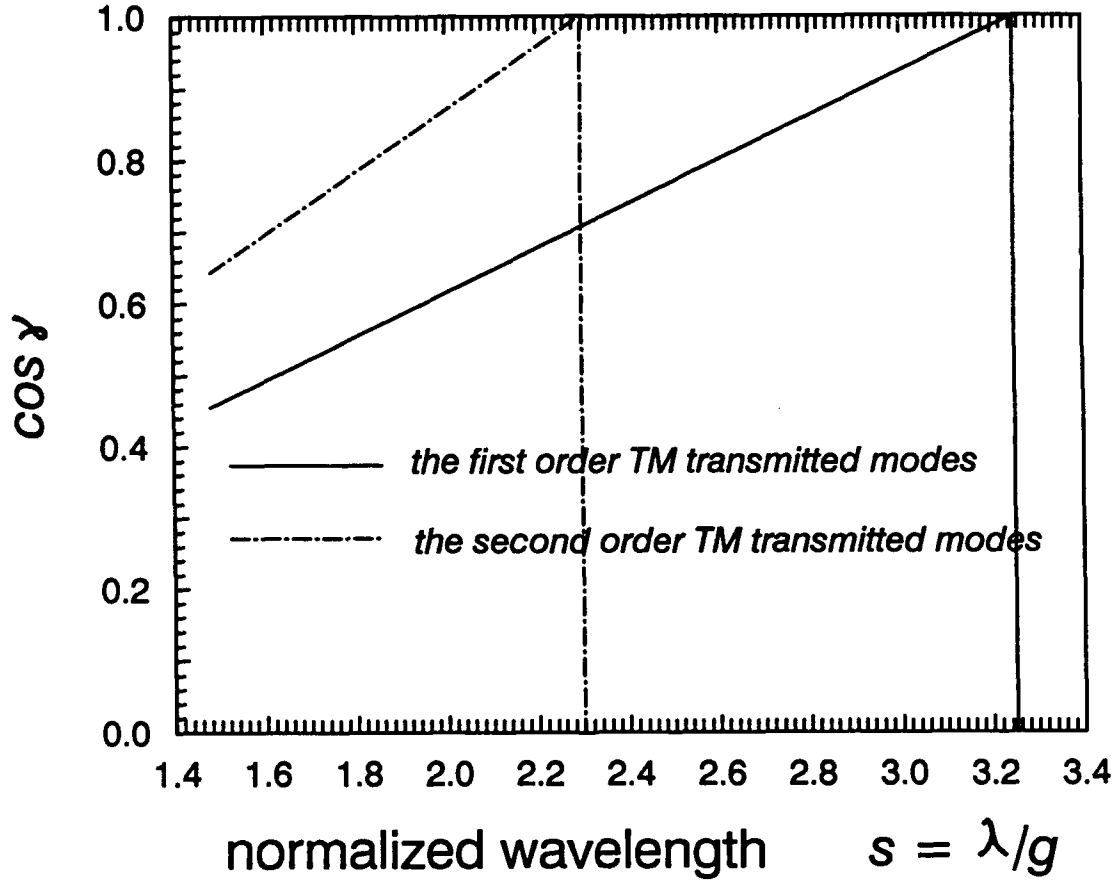

Figure 5 Cosine of the angle between the electric field vector and the normal of quantum well layers versus normalized wavelength.

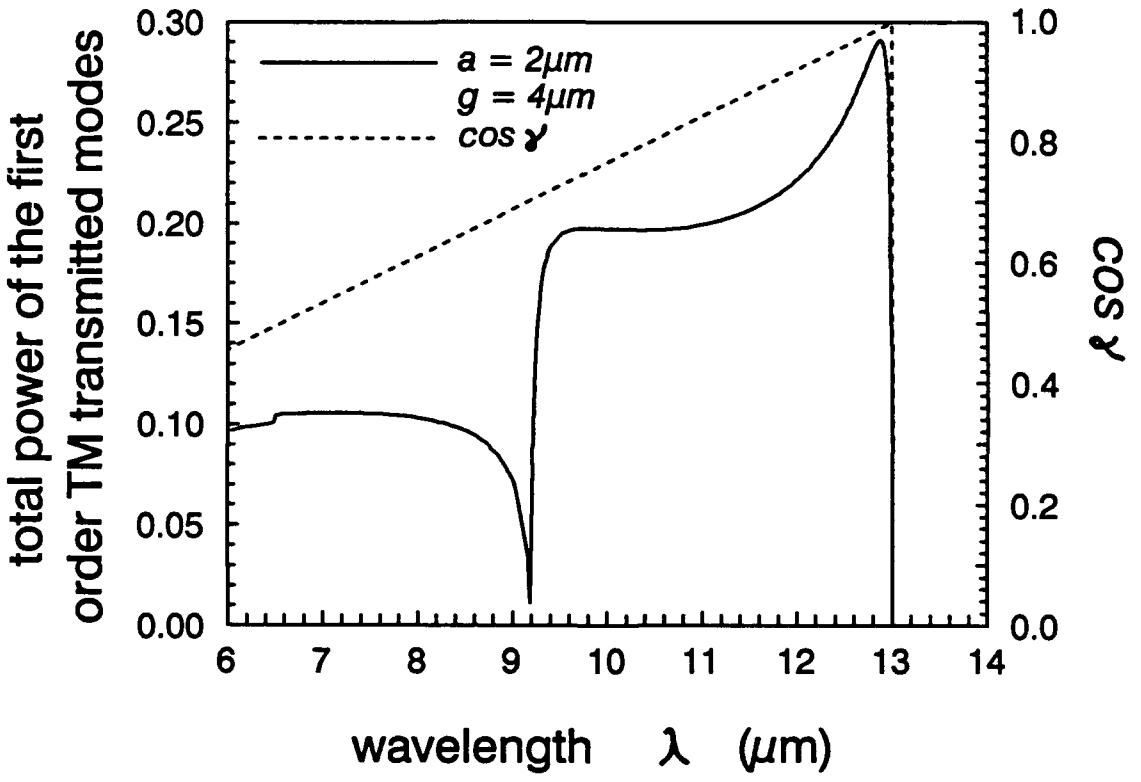

Figure 6 Replot of Fig. 3 and Fig. 5 versus wavelength for g=4.0 μm and a=2.0 μm.

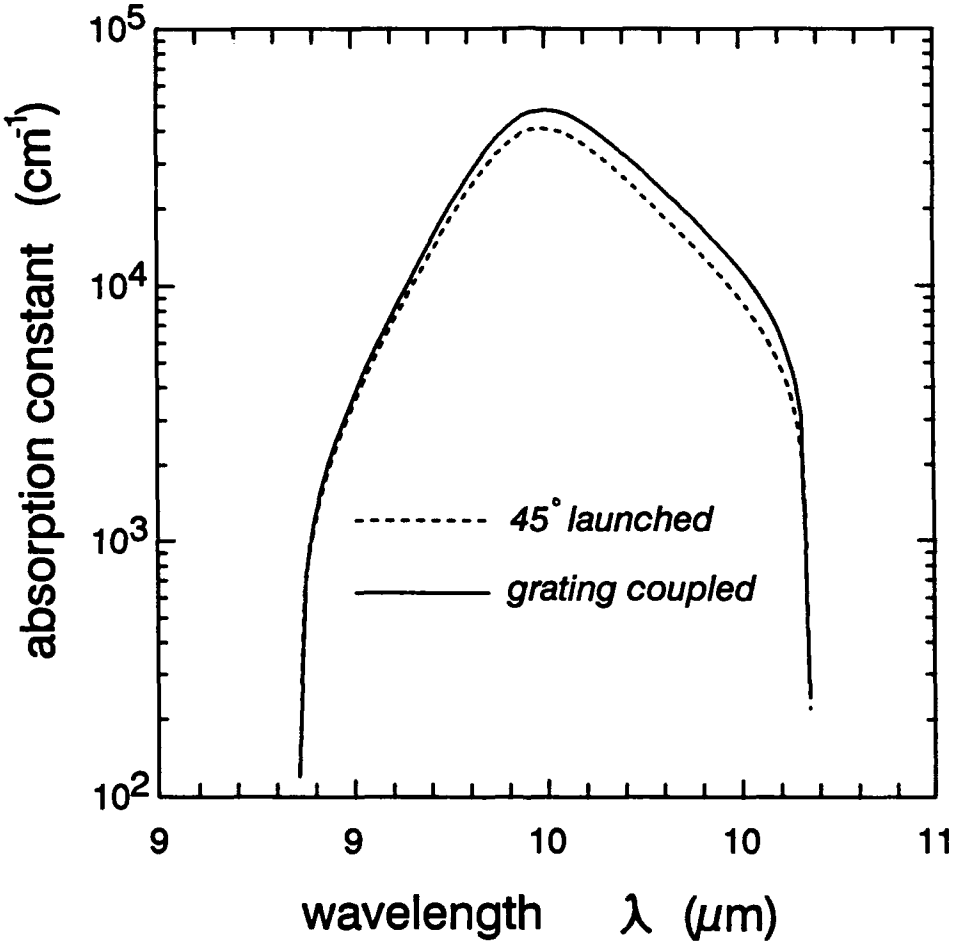

(a)

Figure 7 (a) Absorption constant of the QWIP shown in Fig. 2 covered with a square mesh metal grating coupler, compared to that of a 45^o polished facet.
(b) Quantum efficiency of a square mesh grating coupled GaAs BTM QWIP.

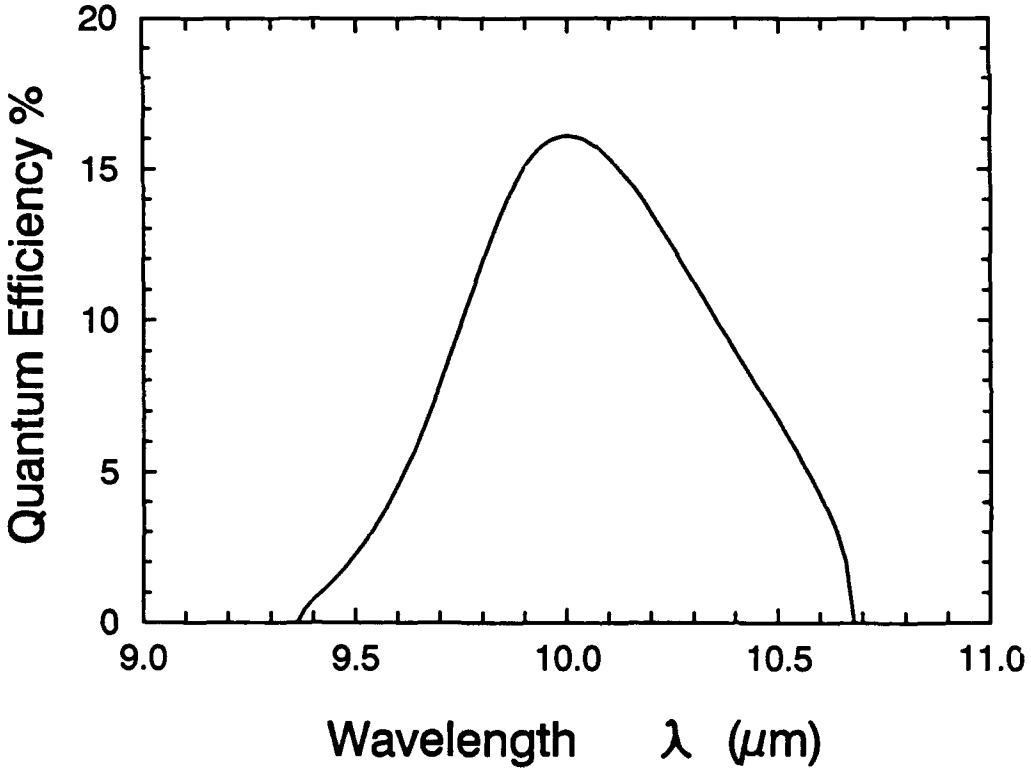

Fig. 7(b)

Quantum efficiency of a square mesh grating coupled GaAs BTM QWIP.

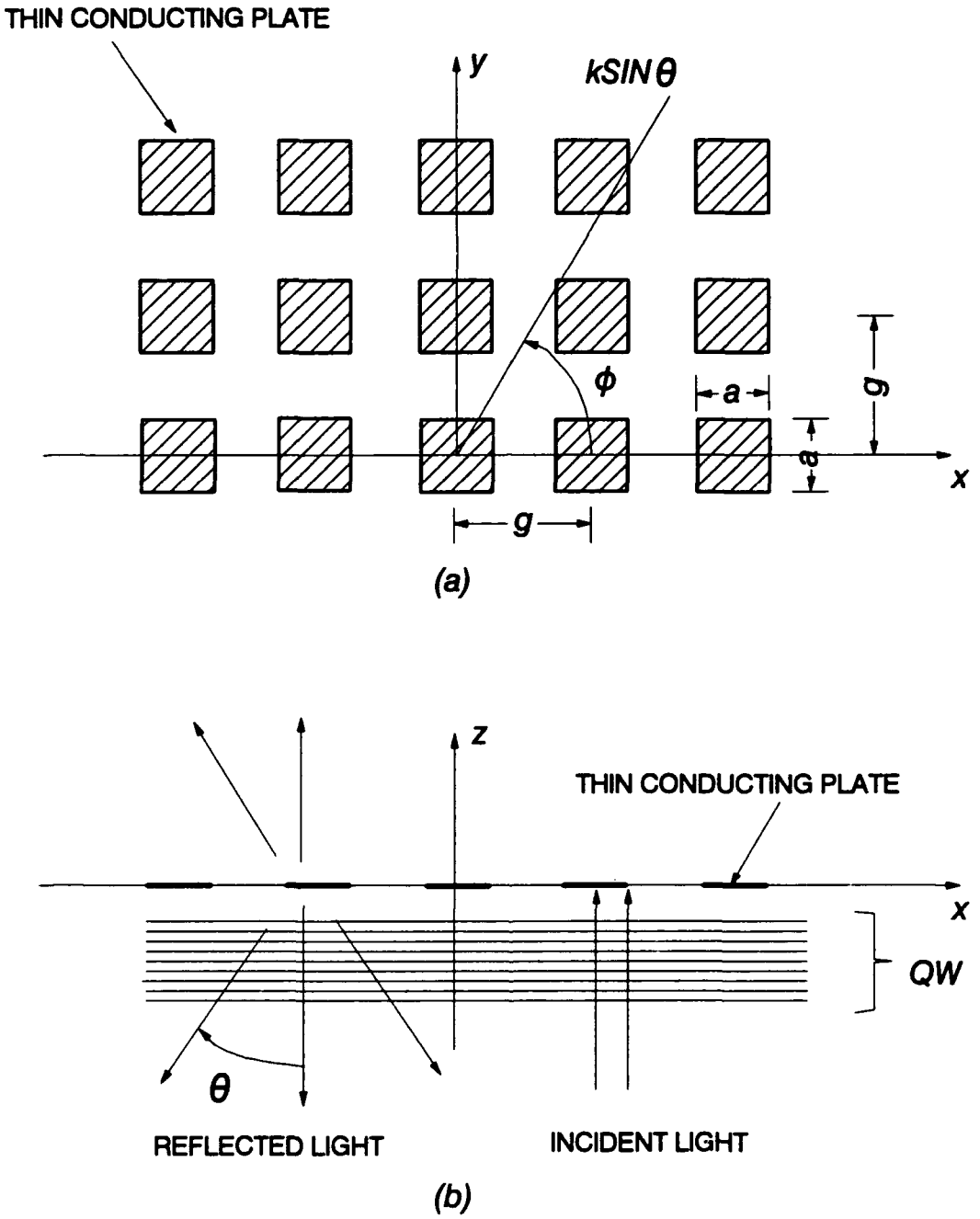

Figure 8 Schematic diagram showing a reflection square cross metal grating and the directions of incident and refracted waves. (a) Top view, and (b) side view.

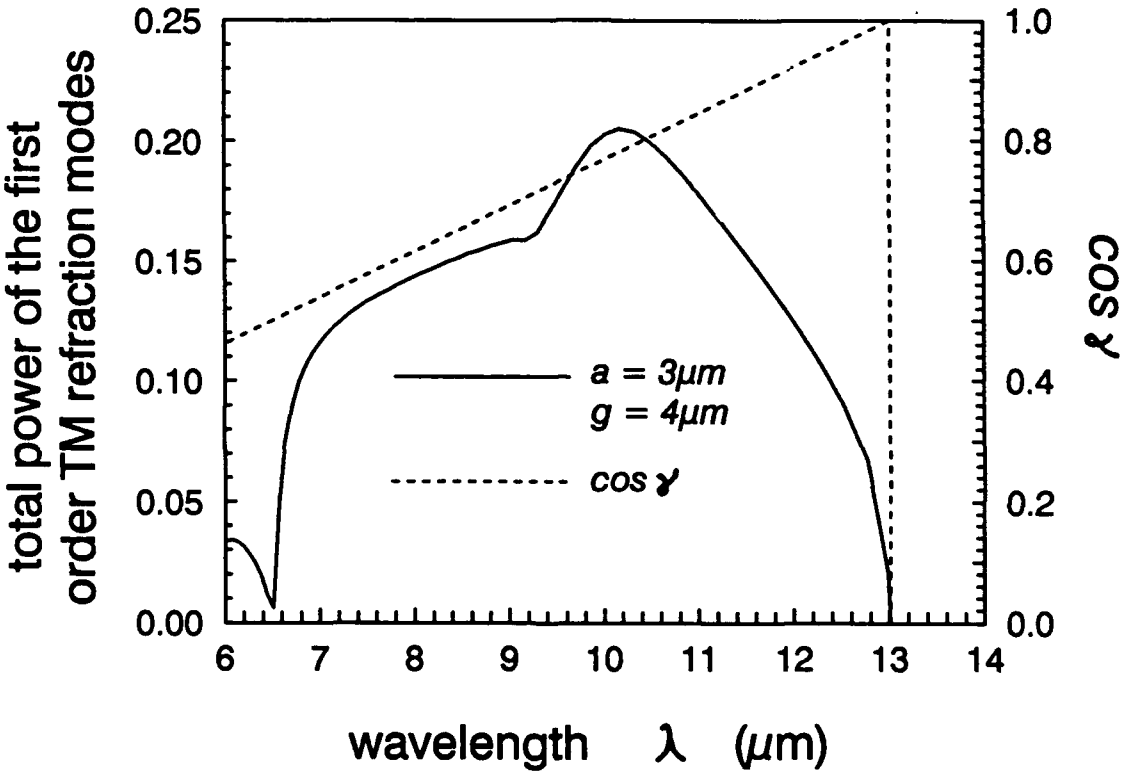

Figure 9 Normalized power of the first order TM refraction waves versus wavelength for g = 4.0 μm and a = 3.0 μm.

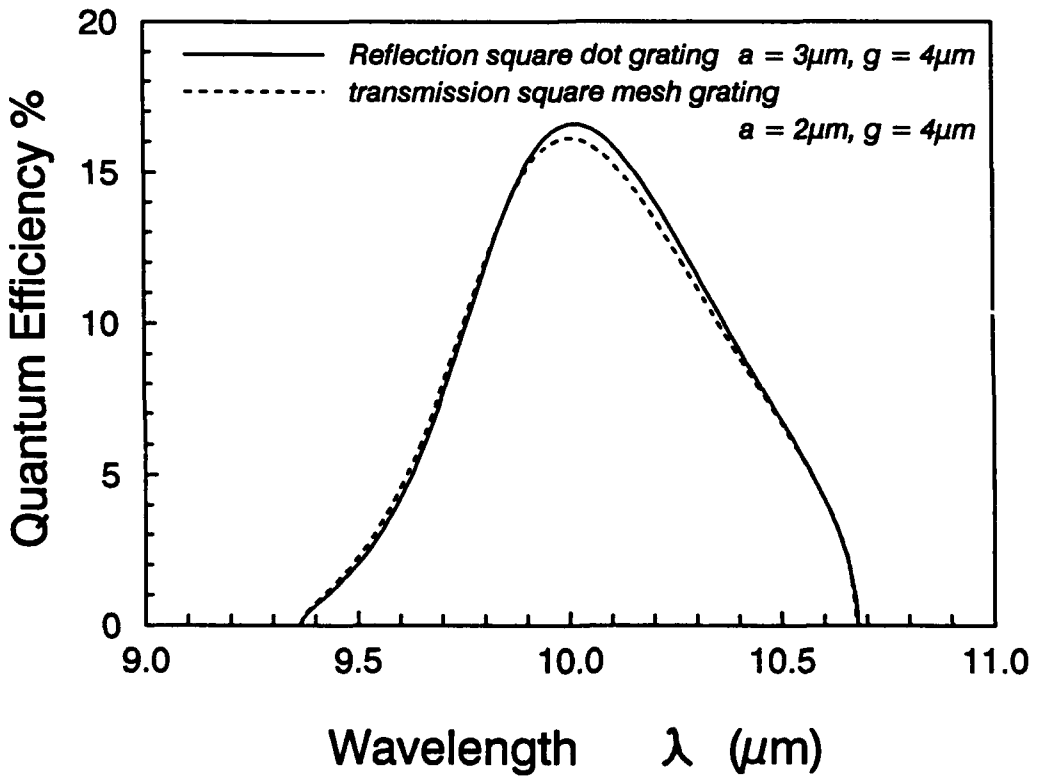

Figure 10 A comparison of the quantum efficiency for a square mesh metal grating and a square cross metal grating coupled GaAs BTM QWIP with same grating period.